

2009

Image-guided port placement for minimally invasive cardiac surgery

Jonathan Marmurek

Follow this and additional works at: <https://ir.lib.uwo.ca/digitizedtheses>

Recommended Citation

Marmurek, Jonathan, "Image-guided port placement for minimally invasive cardiac surgery" (2009).
Digitized Theses. 4285.
<https://ir.lib.uwo.ca/digitizedtheses/4285>

This Thesis is brought to you for free and open access by the Digitized Special Collections at Scholarship@Western. It has been accepted for inclusion in Digitized Theses by an authorized administrator of Scholarship@Western. For more information, please contact wlsadmin@uwo.ca.

Image-guided port placement for minimally invasive cardiac surgery
(Thesis format: Monograph)

by

Jonathan Marmurek

Faculty of Engineering
Graduate Program in Biomedical Engineering

Submitted in partial fulfillment
of the requirements for the degree of
Master of Engineering Science

School of Graduate and Postdoctoral Studies
The University of Western Ontario
London, Ontario, Canada

December 2009

© Jonathan Marmurek, 2009

THE UNIVERSITY OF WESTERN ONTARIO
SCHOOL OF GRADUATE AND POSTDOCTORAL STUDIES

CERTIFICATE OF EXAMINATION

Supervisor

Dr. Terry Peters

Supervisory Committee

Dr. Roy Eagleson

Dr. Bob Kiaii

Dr. Rajni Patel

Examiners

Dr. Daniel Bainbridge

Dr. David Holdsworth

Dr. Hanif Ladak

The thesis by

Jonathan Marmurek

entitled:

Image-guided port placement for minimally invasive cardiac surgery

is accepted in partial fulfillment of the
requirements for the degree of
Master of Engineering Science

Date _____

Chair of the Thesis Examination Board

Abstract

Minimally invasive surgery is becoming popular for a number of interventions. Use of robotic surgical systems in coronary artery bypass intervention offers many benefits to patients, but is however limited by remaining challenges in port placement. Choosing the entry ports for the robotic tools has a large impact on the outcome of the surgery, and can be assisted by pre-operative planning and intra-operative guidance techniques. In this thesis, pre-operative 3D computed tomography (CT) imaging is used to plan minimally invasive robotic coronary artery bypass (MIRCAB) surgery. From a patient database, port placement optimization routines are implemented and validated. Computed port placement configurations approximated past expert chosen configurations with an error of 13.7 ± 5.1 mm. Following optimization, statistical classification was used to assess patient candidacy for MIRCAB. Various pattern recognition techniques were used to predict MIRCAB success, and could be used in the future to reduce conversion rates to conventional open-chest surgery. Gaussian, Parzen window, and nearest neighbour classifiers all proved able to detect 'candidate' and 'non-candidate' MIRCAB patients. Intra-operative registration and laser projection of port placements was validated on a phantom and then evaluated in four patient cases. An image-guided laser projection system was developed to map port placement plans from pre-operative 3D images. Port placement mappings on the phantom setup were accurate with an error of 2.4 ± 0.4 mm. In the patient cases, projections remained within 1 cm of computed port positions. Misregistered port placement mappings in human trials were due mainly to the rigid-body registration assumption and can be improved by non-rigid techniques. Overall, this work presents an integrated approach for: 1) pre-operative port placement planning and classification of incoming MIRCAB patients; and 2) intra-operative guidance of port placement. Effective translation of these techniques to the clinic will enable MIRCAB as a more efficacious and accessible procedure.

Keywords: minimally invasive surgery, robotic coronary artery bypass, image-guidance, port placement optimization, statistical candidacy classification, intra-operative registration, laser projection

Acknowledgments

I'd like to express my sincere gratitude to the following people and organizations:

- My supervisor Dr. Terry Peters for his consistent encouragement, patience, and guidance.
- My committee members Drs. Roy Eagleson and Rajni Patel for their support and advice, and Dr. Bob Kiaii for his willingness to try new things in the OR.
- Dr. Ian Ross, for his enthusiastic involvement and professional help in conducting pre-operative patient imaging experiments.
- Dr. Gerard Guiraudon for his experienced insight and creative spirit.
- The students and staff of my research group for their assistance with my work. In particular Chris Wedlake and John Moore for their help in technical development, and Usaf Aladl for his help with image reconstruction.
- Robarts Research Institute and The University of Western Ontario Biomedical Engineering program, who provided a collegial peer group and work environment.
- The close friends that I made in London, with whom I spent the rest of my days.
- My parents, for always believing in me.
- The annual Medicine Meets Virtual Reality meeting and Studies in Health Technology and Informatics for sharing published material in Appendix A. Also note, material from Chapters 2,3, and 4 is under preparation for submission to the International Journal of Computer Assisted Radiology and Surgery.
- The Canadian Institutes of Health Research and the Heart and Stroke Foundation of Ontario for funding this research.

Table of Contents

Certificate of Examination	ii
Abstract	iii
Acknowledgments	iv
List of Tables	viii
List of Figures	ix
List of Abbreviations	x
Chapter 1 – Introduction	1
1.1. Port placement in minimally invasive surgery	1
1.2. Local history	1
1.2.1. Evolution of port placement planning	2
1.2.2. Causes of MIRCAB failure	2
1.3. Needs for port placement	3
1.4. Existing work	3
1.4.1. Optimal port placement planning	3
1.4.2. Virtual and augmented reality environments	4
1.5. Contribution	5
1.6. Specific motivation	5
1.6.1. Coronary artery disease	5
1.6.1.1. Epidemiology	6
1.6.1.2. Pathogenesis	6
1.6.1.3. Diagnosis and treatment	6
1.6.2. Coronary artery bypass graft surgery	7
1.6.2.1. Conventional open-chest surgery	7
1.6.2.2. Minimally invasive coronary artery bypass surgery	8
1.6.2.3. Manual port placement in MIRCAB	10
1.6.2.4. Current state of MIRCAB	10
1.7. Proposed solution overview	11
1.7.1. Pre-operative planning: patient candidacy and port placement optimization	11
1.7.2. Intra-operative guidance: image-guided laser projection for port placement	12
1.8. Thesis organization	13
1.9. Opportunity and impact	13
Chapter 2 – Problem definition	15
2.1. System overview	15
2.2. Pre-operative planning	15
2.2.1. Image acquisition	15
2.2.2. Optimal port placement	16

2.2.2.1. Database training	18
2.2.2.2. Minimum error port placement optimization	19
2.2.3. Patient candidacy classification	21
2.2.3.1. Statistical classification of patient candidacy	21
2.2.3.2. State of nature: a-priori probabilities	23
2.2.3.3. Class-conditional probabilities	24
2.2.3.4. Bayes' decision rule	24
2.2.3.5. Bayesian risk with multiple features	25
2.2.3.6. Two-category risk-based classification	26
2.2.3.7. Minimum error rate classification	26
2.2.3.8. Discriminant functions and decision boundaries	27
2.2.3.9. The normal density	28
2.2.3.10. Normal density discriminant functions	28
2.3. Intra-operative guidance	29
2.3.1. Registration	29
2.3.2. Laser projection	31
2.3.3. Error assessment	32
2.4. Post-operative database management	32
2.5. Summary of goals	33
Chapter 3 - Pre-operative planning: Port placement optimization and patient candidacy classification	34
3.1. Pre-operative planning overview	34
3.2. Experiments: Optimal port placement	34
3.2.1. Pre-operative CT imaging	34
3.2.2. The patient population	35
3.2.3. Extraction of patient feature geometry	36
3.2.4. Port placement optimization	36
3.2.5. Optimization implementation and testing	36
3.3. Results: Optimal port placement	39
3.4. Experiments: Patient candidacy classification	41
3.4.1. Reduction of important feature geometries	41
3.5. Results: Patient candidacy classification	43
3.5.1. Gaussian candidacy classification	43
3.5.2. Parzen window candidacy classification	45
3.5.3. Nearest neighbour candidacy classification	46
3.5.4. Classifier comparison	47
3.6. Pre-operative planning summary	48
Chapter 4 – Intra-operative guidance: laser projection for port placement	50
4.1. Intra-operative guidance overview	50
4.2. Image guidance system validation	51
4.2.1. 2D vs. 3D image guidance: phantom manual port placement	51
4.2.1.1. Experiments	51
4.2.1.2. Results: Registration error	53

4.2.1.3. Results: Port placement target error	53
4.2.2. Image-guided phantom laser projection	54
4.2.1.1. Experiments	54
4.2.2.2. Results: Registration and port placement error	56
4.2.3. Human vs. laser performance	57
4.3. Operating room evaluation: Human case studies	57
4.3.1. Pre-operative imaging	58
4.3.2. Experiments: Intra-operative registration and port projection	59
4.3.3. Results: Intra-operative registration and port projection	60
4.4. Intra-operative guidance summary	62
Chapter 5 – Conclusions and future work	63
Appendix A – Research ethics approval	66
Appendix B – Publication release	68
References	78
Vita	82

List of Tables

2.1 – Notation for port placement geometry	17
3.1 – Patient population summary	35
3.2 – Port placement optimization error summary	40
3.3 – Gaussian classification summary	44
3.4 – Parzen window classification summary	46
3.5 – k-Nearest neighbour classification summary	47
4.1 – 2D vs. 3D image-guided manual port placement error summary	54
4.2 – Patient case study laser projection error summary	62

List of Figures

1.1 – Coronary artery bypass graft (CABG) surgery	7
1.2 – Conventional open-chest vs. minimally invasive CABG	8
1.3 – The Da Vinci surgical robot	9
1.4 – Block schematic for planning and guiding port placement	12
2.1 – 3D Pre-operative CT imaging	16
2.2 – Port-placement geometry	18
2.3 – Port grid and target sites	19
2.4 – General pattern classification scheme	22
2.5 – Density functions of a single feature	23
2.6 – Posterior probabilities for Bayes' decision rule	25
2.7 – Two-class decision regions for 1D normal distributions	30
2.8 – Two-class decision regions for 2D normal distributions	30
3.1 – Leave-one-out port placement optimization	37
3.2 – Collision detection requirement for port admissibility	38
3.3 – Optimization search space	38
3.4 – Computed vs. expert selected optimal port placement	40
3.5 – Leave-one-out flow diagram for patient candidacy classification	42
3.6 – Gaussian class-conditional feature densities	43
3.7 – Parzen window density estimation for one feature	46
4.1 – Intra-operative image-guidance system diagram	50
4.2 – The cardiothoracic phantom	51
4.3 – 2D and 3D presentations for port placement	52
4.4 – Fiducial landmark registration	53
4.5 – Manual vs. image-based target registration	54
4.6 – Image-guided laser projection test bed	55
4.7 – Laser projected port placement on the phantom	56
4.8 – Laser projection port placement directional error	57
4.9 – Pre-operative fiducial markers and port placement on a patient	59
4.10 – Intra-operative registration routine	60
4.11 – Intra-operative laser projection for port placement	61

List of Abbreviations

1D	One Dimensional
2D	Two Dimensional
3D	Three Dimensional
AR	Augmented Reality
CABG	Coronary Artery Bypass Graft
CAD	Coronary Artery Disease
CT	Computed Tomography
ECG	Electrocardiogram
FOV	Field of View
FRE	Fiducial Registration Error
IGS	Image-Guided Surgery
LAD	Left Anterior Descending
LCX	Left Circumflex
LIMA	Left Internal Mammary Artery
LITA	Left Internal Thoracic Artery
MI	Myocardial Infarction
MIRCAB	Minimally Invasive Coronary Artery Bypass Graft
MIS	Minimally invasive surgery
MRI	Magnetic Resonance Imaging
OR	Operating Room
RCA	Right Coronary Artery
TRE	Target Registration Error
UWO	The University of Western Ontario

Chapter 1. Introduction

1.1. Port placement in minimally invasive surgery

Minimally invasive surgery (MIS), performed using laparoscopic or robotic instruments, is gaining popularity for use in a number of therapeutic procedures. Widespread practice of MIS, however, is limited by the lack of robust and flexible procedures for jointly planning and guiding optimal port placement: the choice of entry points through which the endoscope and operating instruments are introduced. The impact of this choice is often crucial to the success of the intervention, and is usually determined by experience. Continuing advances in the quality of medical image acquisition, remote tracking systems which can record motions of patients and surgical instruments, and computational methods have afforded the opportunity to develop Image Guided Surgery (IGS) systems to assist surgeons. In MIS, systems that guide the surgeon based on patient image data have the potential to optimize the intervention by ensuring that selected port positions will enable access to all surgical sites required to complete the operation. In concert with the image-based port placement presented in this thesis, optimization constraints imposed by robot kinematics can be overcome in future developments toward precise mechatronic instrument manipulation.

1.2. Local history

The first reported minimally invasive robotic coronary artery bypass (MIRCAB) was performed at The University of Western Ontario (UWO) in 1998 [1]. Since then, several research groups worldwide, most notably that of Coste-Maniere, have developed routines for port placement optimization [2,3] in MIRCAB. These methods have focused on optimizing port placement from the robot's perspective. In general, a grid of possible intercostal port positions and the surgical target locations are extracted from 3D image information (CT or MRI). Port configurations (identifying coordinates for three ports: one endoscope, and two instruments) are then scored according to how similar their geometries are to past operations, and on the ability of the robot to reach all the required positions throughout the operation.

1.2.1. Evolution of port placement planning

Prior to this work, the UWO robotic surgical team had not implemented any automated port placement routines, but nonetheless had completed over one hundred MIRCAB operations [4]. The patient-to-patient anatomical variation allowed the team to develop a clinical appreciation for the factors most responsible for successful port placement and surgery. Before 2005, the only pre-operative images used at UWO to plan MIRCAB were bi-plane chest x-rays and dynamic contrast angiograms. While these images provided the surgeon with 2D information on the general location of the blockages required to be bypassed, they lacked any 3D context within which the surgeon could plan where to place the ports to access the surgical targets.

In 2005, at the onset of the present work, multi-slice 2D computed tomography (CT) images were acquired pre-operatively for all MIRCAB patients. In each patient case, the blockage site was located, and its coordinates relative to potential port entry sites were indexed from the images. Still, the surgical team would manually mark the port configuration in the OR since practiced experience exceeded the development of any available IGS system. Of 52 cases where pre-operative CT was collected (during this work), manual port placement was generally successful, but failed in three patient cases (~6 % conversion rate). Prior to collection of pre-operative CT, 10 of 63 (~16 %) cases required conversion. The failed cases required conversion to conventional open-chest heart surgery where consequences may include: morbidity, longer recovery, increased chances of wound infection, sternal dehiscence (tearing of sternum as stainless steel sutures come apart), stroke, and death.

1.2.2. Causes of MIRCAB failure

Failures in MIRCAB operations due to inappropriate port placement were attributed to two main factors: lack of intra-thoracic space; and patient-robot or robot-robot collision. In the latter cause, robotic arms collide with the patient or other robot components and as a result the robot cannot be positioned to reach its targets. This cause of failure is the central issue addressed by existing port placement optimization methods [5,6]. In the first cause of failure, confined or disproportionate intra-thoracic space prevents the surgeon from manipulating the robotic instruments with sufficient dexterity

to perform the operation. To date, no image based port placement procedures evaluate intra-thoracic space during pre-operative planning.

1.3. Needs for port placement

Existing port placement optimization methods do not quantify patient candidacy; rather, they always suggest a patient-specific optimal port configuration. Metrics assessing the intrathoracic space can be evaluated entirely from 3D image-based geometric features to aid with port placement. Comparison of current patient geometries with past patient databases could enable novel means for pre-operative image-based selection of candidate MIRCAB patients in conjunction with computation of optimal port positioning.

Commitment to port placement requires intra-operative methods to accurately map port locations computed from pre-operative images to the patient's chest in the OR. Once anaesthetized for surgery, the patient's muscles relax completely; hence, the patient position on the imaging bed and on the operating table is never identical. Augmented reality systems that integrate pre-operative images, remote tracking data, and display technologies, have the potential to accurately register and present port placement configurations.

To address these issues, this thesis attempts to find answers to the following two connected problems:

- 1) **How to select candidate MIRCAB patients from pre-operative images;** and,
- 2) **How to intra-operatively map port placement configurations.**

Successful selection of candidate MIRCAB patients along with accurate mapping of port positions onto the patient in the OR will ultimately reduce failure rates of MIRCAB operations. Standardization of such expert-trained systems may enhance the utilization of minimally invasive robotic techniques.

1.4. Existing work

1.4.1. Optimal port placement planning

Current methods in port placement have focused on the modeling of optimization algorithms to determine the best incision sites for a patient-specific case. Adhami et al.

[2] define an optimization problem based on indices of tool dexterity, visibility, target reachability, and surgeon comfort, and have shown successful results on porcine trials. Specifically tuned for a Coronary Artery Bypass Graft (CABG) procedure, the optimization problem was refined by Selha et al. [3] such that port configurations attempt to match experimentally determined preset geometries. Here, a grid of port locations is manually selected over the intercostal spaces. All possible port configurations are then scored based on their deviations from past successful surgical manipulator arrangements. Cannon et al. [7] also developed a port selection algorithm that assigns a deviation error metric to port configurations based on experienced optimal geometries. However, this routine still required expert surgeons to approve a list of potential port triads to be assessed.

Another port placement selection algorithm [5,6] focuses on optimizing the robot dexterity for ease of maneuverability while ensuring no robot-patient collision, but does not account for any image-based features specific to a patient's internal anatomy. To facilitate locating critical internal anatomy for MIRCAB, an intra-operative image-based registration technique to overlay the coronary artery tree in the endoscope field of view was proposed by Devernay et al. [8]. This method, however, does not consider changes in a patient's external anatomy between imaging and surgery, and thus the relative coordinates for port placement and the internal anatomy are not registered. Falk et al. [9] address this registration issue by pointing the tele-manipulator tips to a set of fiducial markers to relate the patient and robot coordinate frames. Assuming a rigid-body transformation, again registration error accrues due to changes in external patient geometry between imaging and surgery. Overall registration accuracy was maintained under 1.5 cm, and was sufficient to successfully proceed with MIRCAB operations. Locally, Turgeon et al. proposed techniques to use intra-operative bi-plane angiography for registering the 3D coronary tree to the patient's anatomy [10].

1.4.2. Virtual and augmented reality environments

Virtual environments have been developed [11,12,13] to display port configurations for robotic cardiac surgery, but these have required manual port selection. Augmented reality (AR) systems designed to superimpose pre-operative planning information on top

of the view of the surgical site have also been developed [14] to directly assist surgeons in addition to a virtual simulation. Glossop et al. [15] designed and tested an AR laser projection system that displayed pre-computed beam patterns for a simulated cranioanatomy, and Sugano et al. [16] have also used lasers in surgery to guide hip arthroplasty. In the current literature, however, AR laser projection systems have not yet been reported for facilitating port placement.

1.5. Contribution

This thesis presents a novel approach to jointly planning and guiding port placement. Our strategies, linked through an augmented reality platform are two-fold: 1) pre-operative classification of candidate patients and computation of optimal port positions; and 2) intra-operative registration and image-guided laser projection for port placement.

Statistical decision theory is used to implement classifiers for identifying candidate MIRCAB patients based on a pre-operative image database of patient trials. Existing port placement optimization algorithms are incorporated into the patient classifiers to select port configurations for MIRCAB on a patient-by-patient basis. In addition, an augmented reality system is developed to enable image-guided registration and superimposing of the entry ports on the patient by laser projection. Pre-operative assessment of the patient classifier is tested retrospectively on patient cases and the port placement optimization algorithms are compared to experienced expert port selections. Finally, the intra-operative accuracy of image-guided laser projection for port placement is validated on phantom and human cases.

1.6. Specific motivation

This section details the causes requiring patients to receive minimally invasive coronary artery bypass operations. Moreover, the clinical procedures for both conventional open-chest CABG surgery and MIRCAB are described to highlight the benefits of the minimally invasive approach.

1.6.1. Coronary Artery Disease

1.6.1.1. Epidemiology

Coronary artery disease (CAD) is the primary cause of heart attacks and stroke and is responsible for nearly one third of Canadian deaths. Every year in Canada, hundreds of thousands of cardiac bypass surgeries are performed, placing over a 22.2 billion dollar burden on the healthcare industry*. Risk factors including family history, age, male gender, smoking, diabetes, and diet are highly associated with the progression of atherosclerosis in the coronary arteries leading to CAD. In order to reduce costs in treatment of the disease by surgery, surgical methods of reduced risk and high efficiency must be identified.

1.6.1.2. Pathogenesis

The coronary arteries deliver oxygenated blood to the myocardial muscle to source the required energy, through ATP production, for the heart to pump. Development of atherosclerotic plaque on the inner lumen of the coronary arteries results from pathological progression through fatty build-ups, fibrotic plaque formation, inflammation of the vessel wall, fibrotic plaque growth and calcification. This pathway can manifest into coronary artery disease - blockage of the coronary arteries ultimately inducing ischemia and myocardial infarction (MI), signified by death of the myocardial muscle tissue due to insufficient blood supply.

1.6.1.3. Diagnosis and treatment

CAD patients present clinically with a history of hypertension (high-blood pressure), angina pectoris (chest pain) and high cholesterol. Following an electrocardiogram (ECG) and blood work, suspect patients are sent for dynamic contrast x-ray angiograms in which catheter injections show the blood flow through the coronary arteries and can reveal the location of a coronary artery blockage. Depending on the severity of the blockage, patients are recommended for treatment either by angioplasty or CABG surgery. Angioplasty is the mechanical widening of the artery achieved by catheter delivery of a stent, a cylindrical metal structure which is forced open by a balloon inside the coronary

* Statistics from www.heartandstroke.com

artery wall. However, more progressive occlusions cannot be widened and must be treated by CABG, in which a vessel external to the heart is surgically fused to the occluded vessel to “bypass” the blockage and provide sufficient blood supply.

1.6.2. Coronary Artery Bypass Graft Surgery

CABG procedures (Figure 1.1) can be performed on any of the three coronary arteries: the left anterior descending (LAD), the left circumflex (LCX), and/or the right coronary artery (RCA). To re-establish blood supply distal to the occlusion, either the saphenous vein from the leg, or more commonly in bypass of the LAD, the left internal mammary artery (LIMA, also referred to as the left internal thoracic artery – LITA) is isolated from the thoracic cavity. For decades this procedure has been performed within the open chest, but recent technological advances have afforded options for minimally invasive approaches, including endoscopic and robotic surgery [17].

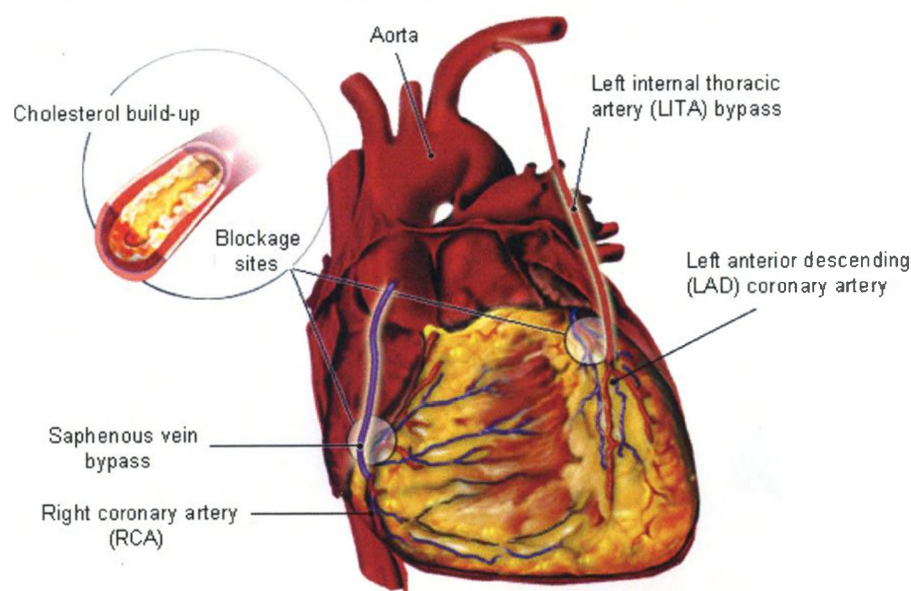


Figure 1.1 – Coronary artery bypass graft (CABG) surgery. In the double bypass shown, the Saphenous vein and LITA are harvested and fused beyond the blockages in the RCA and LAD coronary artery. Note the LCX is not shown – it travels behind the heart[†].

1.6.2.1. Conventional open-chest surgery

Following anaesthetization through intravenous lines and mechanical ventilation support through a secured endotracheal tube, the conventional CABG procedure begins

[†] Modified from www.worldmedassist.com

with a median sternotomy. A long (approximately 10 inch) incision is made along the sternum using a saw blade, and the sternum itself is divided to expose the heart. A heart-lung machine is used for the operation to pump blood and ventilate for the patient. This stopping and starting of the heart and lungs is associated with several risks including stroke, renal failure, atrial fibrillation, need for blood transfusion, systemic inflammatory response, and death. The major surgical steps comprising the CABG procedure then follow most commonly as: stopping the heart, exposing the occluded vessel (e.g., LAD) through incision and removal of epicardial tissue; harvesting of the artery to be used for bypass (e.g., LIMA); cleaving of the LIMA, and anastomosis - fusion of the LIMA to the LAD by suture beyond the occlusion. Patients are sent to the intensive care unit and typically remain in hospital for five to six days. Accompanying the traumatic response to the open-chest operation is high blood loss, heavy scarring, and heightened risk of infection and sternal dehiscence. Patients often experience weakness for weeks to months post operation with prolonged recovery time.

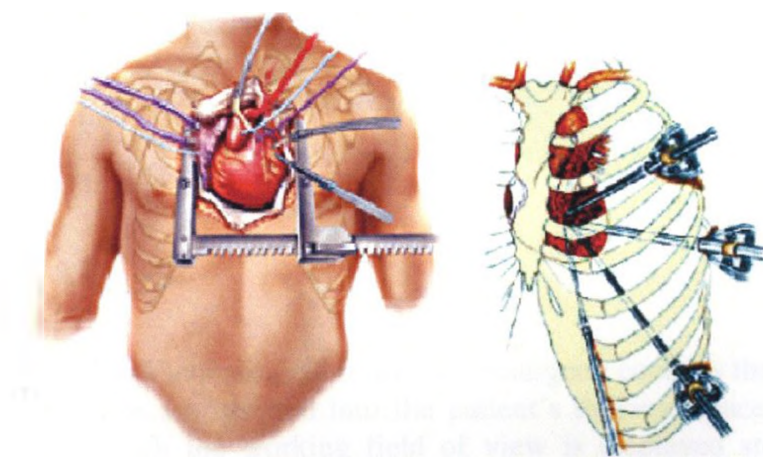


Figure 1.2 – Conventional open-chest vs. minimally invasive CABG. Left: Traditional open-chest surgery; Right: Minimally invasive access through entry ports 1 cm in diameter. (*biomed.brown.edu*)

1.6.2.2. Minimally invasive robotic coronary artery bypass surgery

The surgical objectives for minimally invasive CABG are identical to the conventional procedure, but access to the internal anatomy is through small incisions (~ 1 cm diameter) made in the intercostal muscles between the patient's ribs (Figure 1.2). In

addition, no heart-lung machine is required [18,19]; the operation is performed on the beating heart with the left lung deflated (to make space for the robotic manipulators). Patients undergo lung function studies beforehand to verify that they can withstand single-lung ventilation. In laparoscopic or robotic (DaVinci Surgical System, Intuitive Surgical, Sunnyvale CA) assisted methods, an endoscope (to provide the surgeon with video feedback of the operating field of view) along with various instruments (for holding, cutting, and grasping tissue) are inserted through the port incisions (Figure 1.3).



Figure 1.3 – The Da Vinci surgical robot[‡]. The surgeon controls the robot from a remote console. Three tools are inserted into the patient's thoracic space, one of which is an endoscope from which the working field of view is displayed stereoscopically to the surgeon's console, and by video overhead the patient bed.

Anastomosis can be either performed totally closed-chest with robotic-assistance (depending on the patient's body and location of the LAD) or through a non rib-spreading 3-5 cm mini-thoracotomy incision. Without the median sternotomy, patients have reduced scarring, less risk of complications, and a faster return to habitual activity [20,21,22]. Despite the attractive benefits of minimally invasive approaches to CABG, the skill and training required to perform these operations given constrained visibility, loss of dexterity

[‡] See www.intusurg.com

and loss of tactile feedback prevent endoscopic and robotic techniques from becoming widespread. Recent advances in robotic instrumentation and image-guidance systems can ultimately ease the challenges of this operation and reduce the morbidity associated with the conversion to conventional CABG.

1.6.2.3. Manual port placement in MIRCAB

Locally, our expert surgeon and radiologist report that port configurations for MIRCAB were generally consistent but varied among patients. Left and right operating tools were commonly inserted through the 2nd, or 3rd (left tool), and 6th or 7th (right tool) intercostal rib spaces. The endoscope port is placed at the apex of a triangle formed usually in the 5th, but sometimes 4th, intercostal space. The incision sites, with robotic tools inserted, must give the surgeon access to operate along the LIMA from 1st to 6th ribs, and down to the LAD underneath the pericardium. The cause of the three MIRCAB failures, requiring conversion to open-chest surgery, was attributed to the patients having too little space inside their chest for the surgeon to perform all the required gestures. This lack of space can be characterized from pre-operative CT images to assess whether patients are candidates for robotic intervention, or whether the conventional open-chest approach is safer. In 2005, at the onset of collecting pre-operative multi-slice CT, intra-thoracic space was assessed by measurements of the pleura-to-heart distance at each incision site. Nevertheless, to date, no quantitative decision rules have been developed to help classify candidate MIRCAB patients. Other groups [23,24] performing MIRCAB without image-guidance have also relied on expert surgeon experience to manually choose port locations, and have likewise not been able to predict conversion rates based on pre-operative imaging. In addition, these manual port placement approaches assume no variation among patients' internal anatomy.

1.6.2.4. Current state of MIRCAB

Learning curves constructed from total operative time in MIRCAB have shown the potential to integrate robotics into cardiac surgery programs, and it has been demonstrated that LIMA takedown times can be reduced from 1.5 hrs to 0.5 hrs after performing ten cases [25]. In other studies on the learning curves of MIRCAB

performance, Oehlinger et al. report [26] that chest size has had little effect on time to harvest the LIMA. But, the effect of thoracic space on failure likelihood or conversion rates is not studied. Locally, Novick et al. [27] report learning curves for MIRCAB operations and comment on the common reasons for conversion to open-chest surgery: difficulty locating and surgically revealing the LAD; inability to tolerate single-lung ventilation; and, inadequate intra-thoracic working space. Locating the LAD can now readily be accomplished using 3D imaging, and lung assessment tests can be administered before operating. Thus, intra-thoracic space remains a key factor in determining candidate patients for MIRCAB. We propose that metrics assessing this working space can be computed from pre-operative images to identify potential subjects. Additionally, aside from the groups discussed above who address image-based port placement strategies, most surgical teams performing MIRCAB are not using image-guidance to effectively assist in port placement, likely due to a lack of methods to standardize this procedure. We address means for jointly planning (pre-operatively) and guiding (intra-operatively) port placement. A virtual environment that enables planning based on a database of past patient geometries is developed in conjunction with optical tracking based registration and laser projection techniques for mapping port positions.

1.7. Proposed solution overview

The identified port placement challenges – *assessing patient candidacy* and *mapping port positions* – are addressed through the development of an augmented reality system comprising computer visualization software (Atamai Viewer [28]), image-databases, optimization and classification algorithms (MATLAB), and an optical tracking system with integrated laser projection (NDI, Traxtal). A block schematic of the proposed system for planning and guidance is profiled in Figure 1.4. The general approaches to both the guidance and planning stages are described thereafter.

1.7.1. Pre-operative planning: patient candidacy and port placement optimization

CT images along with post-operative assessment of the surgical outcomes form a database used to predict surgical success based on pre-operative imaging data of future patients. By associating quantitative geometric features extracted from pre-operative

images with either *successful* or *failed* MIRCAB cases, implemented statistical classifiers, parametric and non-parametric, are trained and tested to identify patients as *candidate* or *non-candidate* cases. Port placement optimization algorithms that compare geometric features from the post-operative database are also implemented. Computed optimal port configurations for each patient are compared retrospectively to the manual expert port configurations, and are tested for candidacy to determine whether the pre-operative optimization and classification routines combined would have predicted failed cases otherwise unidentified by an expert surgeon.

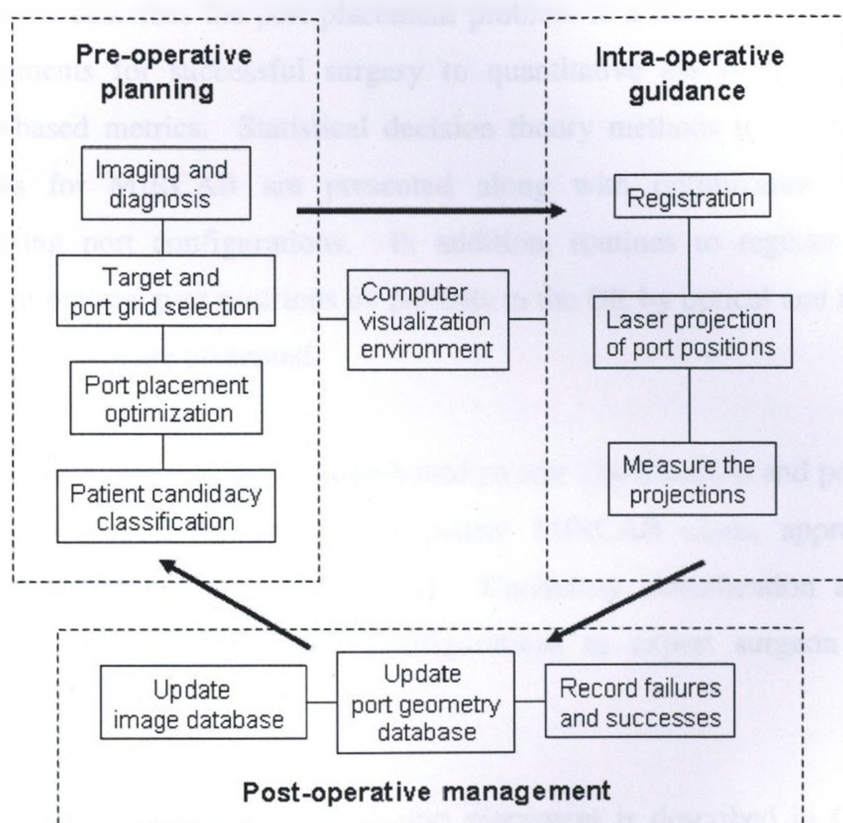


Figure 1.4 - Block schematic for planning and guiding port placement

1.7.2. Intra-operative guidance: image-guided laser projection for port placement

The image guidance system integrates computer visualization software with tracking and laser projection devices through an advanced programming interface. The fidelity with which computed port positions can be mapped to a patient is tested on both phantom and human cases. Point-based registration routines relate the tracking and imaging

coordinate systems, and a laser projector is then driven to display the computed port positions directly on the subject. Measured port projections are compared to computed positions to validate the accuracy of the image-guided laser projection. Further comparison of manual, laser projected, and computer optimized port placement on human trials ensures that the port projection accuracy sufficiently estimates expert port placement configurations.

1.8. Thesis organization

- *Chapter 2* describes the port placement problem in a framework relating clinical requirements for successful surgery to quantitative assessments of geometric image-based metrics. Statistical decision theory methods to classify candidate patients for MIRCAB are presented along with optimization methods for computing port configurations. In addition, routines to register and display resultant optimal port positions on patients in the OR by optical and image guided laser projection are presented.
- In *Chapter 3*, pre-operative image-based patient classification and port placement optimization is tested on clinical patient MIRCAB cases, approved by the research ethics board (Appendix A). Candidacy classification accuracy and comparison of computed port configurations to expert surgeon records are detailed.
- Image-guided laser projection for port placement is described in *Chapter 4* by way of intra-operative demonstrations on phantom and human MIRCAB cases. The accuracy of the port placement indicated by the proposed augmented reality system is presented in detail.
- *Chapter 5* concludes the thesis with a discussion of limitations, suggestions for improvement, and the benefit of application.

1.9. Opportunity and impact

Image-based assessment of patient candidacy and optimization of port placement configurations from past trials, combined with intra-operative laser projection guidance for localizing computed port locations, affords enhanced methods for planning and executing minimally invasive robotic surgery. The approaches developed herein are specific to MIRCAB, but the methods may be generalized for any minimally invasive intervention. The penetration of MIRCAB as a surgery option has been limited by the required skill for the operation: image-guidance systems could facilitate these procedures. Ultimately, the joint image-based planning and guidance system will ease the challenges of selecting patients, choosing port configurations, and mapping port placement plans in the OR. Use of the pre-operative planning modules in future trials has the potential to identify non-candidate patients, relieving the burden of conversion to conventional open-chest surgery. Additionally, the use of intra-operative laser projection guidance for port placement will ensure accurate execution of pre-operative port placement plans. These advancements provide an opportunity to facilitate the training of new robotic surgeons by universally standardizing port placement planning and guidance. Both expert surgeons and surgeons at remote locations could equally perform minimally invasive operations by either on-site or tele-manipulated surgical robotics.

Chapter 2. Problem Definition

2.1. System overview

This chapter presents an integrated solution for using pre-operative images to assist planning and guidance of MIRCAB surgery. In planning the surgery, port configuration geometries for successful access to all surgical targets are computed according to an optimization metric that compares the current patient to a past patient database. Subsequently, the candidacy of each new patient is assessed using pattern recognition techniques, predicting success or failure of MIRCAB given the current patient's optimal port configurations. Following pre-operative port placement optimization and classification, the ports must be mapped accurately to the patient's anatomy in the operating room. Intra-operative guidance is achieved by registering the patient's physical anatomy to the image dataset using optical tracking, and the port locations are displayed directly on the patient using laser projection. Assessment of the error in port placement projections follows to validate the system.

2.2. Pre-operative planning

2.2.1. Image acquisition

Multi-slice images, collected pre-operatively, provide a 3D CT image dataset to plan each patient's MIRCAB intervention. For the examples presented in this thesis, images are acquired from a 4-slice spiral CT scanner (GE Medical Systems, Milwaukee, WI). CT was chosen because the images reveal all critical anatomy required for port placement planning: the heart, the LAD blockage site, the LITA, and the rib structure. The images are formatted into MINC files [29] to allow tri-plane manipulation of the data in the Atamai image viewer [28]. In order to visualize the anatomy in a 3D context, surfaces of the rib structure and the skin are segmented using the marching cubes algorithm [30]. Figure 2.1 illustrates typical pre-operative patient image data and identifies the critical anatomy for planning MIRCAB.

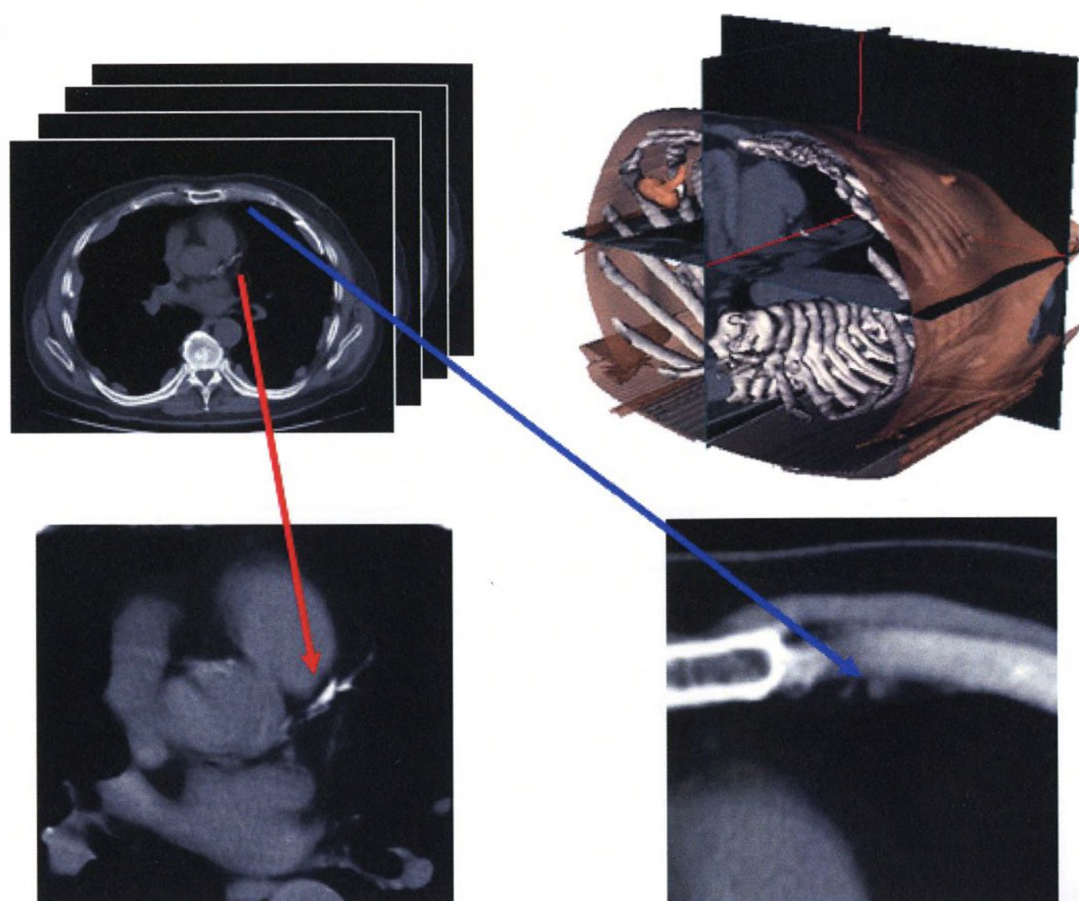


Figure 2.1 - 3D Pre-operative CT imaging. *Top*: Multi-slice CT images are converted into an interactive 3D tri-plane volume with segmented ribs and skin. *Bottom*: Focusing in on the heart reveals the LAD blockage site (*red arrow*); and, a trained eye can localize the LITA (*blue arrow*) used for bypass.

2.2.2. Optimal port placement

Port placement optimization is achieved through implementation of a variation on minimum-error based algorithms presented in the literature [2,3,7]. Before any algorithmic approach can be executed, the routine requires a database of patient images to summarize geometric features representative of successful past manual port placement approaches. In this database, the image coordinates of the expert-chosen three port locations (left and right surgical tools, and endoscope), and of three critical target sites (LAD blockage site, and the superior and inferior ends of the LITA for takedown) are recorded for each patient. The three port positions and the target position form a unique

pyramid with an apex at each of the three target sites, and each pyramid configuration can be summarized geometrically by: port-to-port distances, port-to-target distances, and angles between instruments. Table 2.1 summarizes the notation used throughout the thesis to describe the port placement geometry, along with corresponding clinical descriptors of the importance of each feature for MIRCAB. These geometric features are used for the database training in the following section. Figure 2.2 profiles the selection of ports and targets for a sample patient and shows the port pyramid geometry formed at one of the target sites.

Table 2.1 – Notation for port placement geometry

Notation	Feature	Significance
<i>Port-to-port distances</i>		
d_{LR}	Distance from left to right tool ports	Must be far enough apart to enable robot positioning and movement of the instruments in the thorax
d_{LE}	Distance from left tool to endoscope port	
d_{RE}	Distance from right tool to endoscope port	
<i>Port-to-target distances</i>		
$d_{L,LAD}$	Distance from left tool port to LAD	Must be far enough apart to allow dextrous control of the instruments, but must be within a reachable distance for the operating tool lengths
$d_{L,iLITA}$	Distance from left tool port to inferior LITA	
$d_{L,sLITA}$	Distance from left tool port to superior LITA	
$d_{R,LAD}$	Distance from right tool port to LAD	
$d_{R,iLITA}$	Distance from right tool port to inferior LITA	
$d_{R,sLITA}$	Distance from right tool port to superior LITA	
$d_{E,LAD}$	Distance from endoscope to LAD	
$d_{E,iLITA}$	Distance from endoscope to inferior LITA	
$d_{E,sLITA}$	Distance from endoscope to superior LITA	
<i>Angles between instruments</i>		
$\alpha_{LR,LAD}$	Angle between L & R instruments at LAD	Should be large enough so that the L and R tools are manoeuvrable and can be seen by the endoscope
$\alpha_{LR,iLITA}$	Angle between L & R instruments at iLITA	
$\alpha_{LR,sLITA}$	Angle between L & R instruments at sLITA	
$\alpha_{LE,LAD}$	Angle between L & E instruments at LAD	
$\alpha_{LE,iLITA}$	Angle between L & E instruments at iLITA	
$\alpha_{LE,sLITA}$	Angle between L & E instruments at sLITA	
$\alpha_{RE,LAD}$	Angle between R & E instruments at LAD	
$\alpha_{RE,iLITA}$	Angle between R & E instruments at iLITA	
$\alpha_{RE,sLITA}$	Angle between R & E instruments at sLITA	

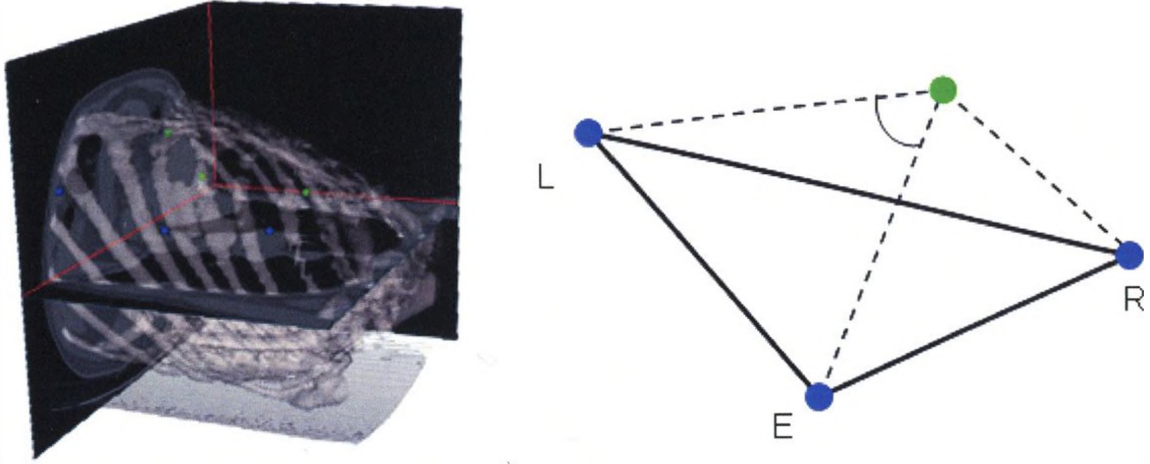


Figure 2.2 – Port placement geometry. *Left*: Expert-chosen port placement positions (blue spheres) and target sites (green spheres) are selected in the image. *Right*: Pyramid formed by the ports and a single target describes port-to-port distances (solid lines), port-to-target distances (dashed lines), and angles between instruments (arc shown for the angle between the left operating tool and the endoscope).

2.2.2.1. Database training

The optimization model is trained based on the expected values for all of the port placement geometric features. From a database of successful MIRCAB port configurations, the optimal value for each feature is computed as the mean for that feature, and upper and lower bounds are imposed at three standard deviations from the mean (i.e. the means and deviations for each distance and angle feature are computed across all patients). A feature vector representing the port configuration geometry for a single patient is denoted as:

$$\mathbf{x} = [d_{LR}, d_{LE}, d_{RE}, d_{L,LAD}, d_{L,iLITA}, d_{L,sLITA}, d_{R,LAD}, d_{R,iLITA}, d_{R,sLITA}, d_{E,LAD}, d_{E,iLITA}, d_{E,sLITA} \dots \alpha_{LR,LAD}, \alpha_{LR,iLITA}, \alpha_{LR,sLITA}, \alpha_{LE,LAD}, \alpha_{LE,iLITA}, \alpha_{LE,sLITA}, \alpha_{RE,LAD}, \alpha_{RE,iLITA}, \alpha_{RE,sLITA}].$$

Port-to-port and port-to-target distances are calculated from the distance between two points:

$$\|\mathbf{p}_1 - \mathbf{p}_2\| = \sqrt{(x_1 - x_2)^2 + (y_1 - y_2)^2 + (z_1 - z_2)^2}, \quad (2.1)$$

where \mathbf{p} represents the x, y, and z coordinates of a port position. Angles between instruments at a particular target are calculated from the dot product definition:

$$\alpha = \cos^{-1} \left(\frac{(\mathbf{p}_1 - \mathbf{t}) \bullet (\mathbf{p}_2 - \mathbf{t})}{\|\mathbf{p}_1 - \mathbf{t}\| \|\mathbf{p}_2 - \mathbf{t}\|} \right), \quad (2.2)$$

where \mathbf{t} represents the x, y, and z coordinates of a target position.

The optimal feature values across a database of N patients are computed as:

$$\mathbf{x}_{\text{opt}} = \frac{1}{N} \sum_{i=1}^N \mathbf{x}_i, \quad (2.3)$$

where \mathbf{x}_i represents the feature vector of the i^{th} patient for $i = 1, 2 \dots N$.

The upper and lower bounds for the features are:

$$\mathbf{x}_u = \mathbf{x}_{\text{opt}} + 3 \sqrt{\frac{1}{N} \sum_{i=1}^N (\mathbf{x}_i - \mathbf{x}_{\text{opt}})^2}, \text{ and } \mathbf{x}_l = \mathbf{x}_{\text{opt}} - 3 \sqrt{\frac{1}{N} \sum_{i=1}^N (\mathbf{x}_i - \mathbf{x}_{\text{opt}})^2}. \quad (2.4a, 2.4b)$$

For each new successful MIRCAB case, the database is updated with the most recent patient geometries, and the optimal and boundary feature vectors are re-trained.

2.2.2.2. Minimum-error port placement optimization

Provided pre-operative images for an incoming MIRCAB case are available, port placement configurations can be optimized according to an objective metric that minimizes error with respect to the trained optimal feature geometries. First, a grid of potential port positions is extracted manually from the patient's 3D image data and the target sites are marked (Figure 2.3). This is the only manual step in the optimization

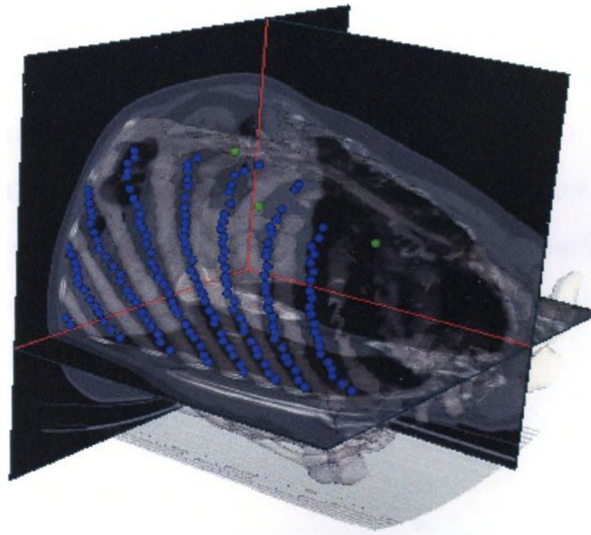


Figure 2.3 – Port grid and target sites. Grid of potential port locations (*blue*) is marked manually along the intercostals. Target locations (*green*) are marked at the LAD, inferior and superior LITA.

procedure. To automate selection of a port grid, coordinates over the segmented skin surface could be used, but this would include port positions not necessarily placed along the intercostal spaces. Alternatively, a distance map extracting lines through the intercostals could be used. Though this approach would eliminate manual interaction for port placement planning, it has not yet been explored and is not the emphasis of this thesis. Furthermore, the target locations will always require marking by an expert radiologist. The image coordinates of the i^{th} potential port location from the manually selected grid are denoted as: $\mathbf{p}_i = [x_{im} \ y_{im} \ z_{im}]$. A list of all possible port configurations from a grid of P ports is then arranged as:

$$\mathbf{P} = \begin{bmatrix} \mathbf{p}_1 & \mathbf{p}_2 & \mathbf{p}_3 \\ \mathbf{p}_1 & \mathbf{p}_2 & \mathbf{p}_4 \\ \vdots & \vdots & \vdots \\ \mathbf{p}_i & \mathbf{p}_j & \mathbf{p}_k \end{bmatrix} \text{ where } i \neq j \neq k.$$

In the port configuration list, the first column denotes port positions of the left surgical tool, the middle column denotes endoscope port positions, and the third column denotes the port positions of the right surgical tool. Each row is thus a port configuration triad. Since it is redundant to include permutations of the left, right, and endoscope tools, the length of the list reduces to $L = \frac{P!}{3!(P-3)!}$.

By iterating through each possible port triad in the list, the port configurations are first marked as '*admissible*' or '*non-admissible*' according to whether their associated feature vectors lie within the upper and lower feature boundaries. Also, '*admissible*' port configurations must provide a collision-free path [2,9] to each target. Then, only the '*admissible*' port locations are scored according to the following error-minimizing optimization objective:

$$\min_{\mathbf{P}_i} \sum_{\text{features}} \text{abs}(\mathbf{x} | \mathbf{P}_i - \mathbf{x}_{\text{opt}}), \quad (2.5)$$

where $\mathbf{x} | \mathbf{P}_i$ is the feature vector computed for the i^{th} possible port configuration. Output from this algorithm provides a list of *admissible* port triads, ranked by their deviation from optimal feature geometries. The port triad with the lowest objective error is then chosen as the optimal port placement configuration for the incoming patient.

2.2.3. Patient candidacy classification

All current port placement optimization routines [2,3,5,6,7], including that described above, naively assume that for every patient requiring CABG there is an optimal port configuration (i.e. whatever port triad provides the lowest objective error score should be the configuration used for that patient). During the course of this work, however, our local expert surgeons experienced three MIRCAB cases (of 52 with pre-operative CT imaging) that required conversion to conventional open-chest CABG in which the cause of failure for these cases was small intra-thoracic space. Failed cases preceding this work did not include pre-operative CT and are not considered in this thesis because intra-thoracic space cannot be assessed. Another reason for conversion is robot-patient or robot-robot collision, but is not the focus of the present image-based geometric feature-based port placement planning. Existing optimization routines examine robot dexterity optimization and collisions in port placement planning [5,6], and should be integrated with the presented image-based approach. Also, other groups performing MIRCAB have documented [31,32,33] conversion rates to conventional open-chest CABG, but have yet to develop image-based quantitative assessments of the causes of MIRCAB failure.

With little room to operate within a small intra-thoracic space, the robotic surgical tools cannot be manipulated to perform the LITA takedown and attachment to the LAD. In this chapter a statistical pattern classification approach is proposed that, following port placement optimization, classifies patients as '*candidates*' or '*non-candidates*' for MIRCAB. In general, the routine associates manual expert-chosen port placement geometries from past cases as '*successful*' or '*failed*'. Statistical decision theory methods can then be used on an incoming CABG patient to classify their candidacy for MIRCAB based on their feature geometries. Detailed in the following section is a novel framework for applying statistical decision methods to patient classification based on pre-operative image data. Figure 2.4 shows a general pattern classification scheme for training classifiers and testing new incoming data.

2.2.3.1. Statistical classification of patient candidacy

The goal of this methodology is to be able to classify incoming CABG patients as either '*candidate*' or '*non-candidate*' for MIRCAB using features associated with optimal port configurations optimized from pre-operative image data. A true difference

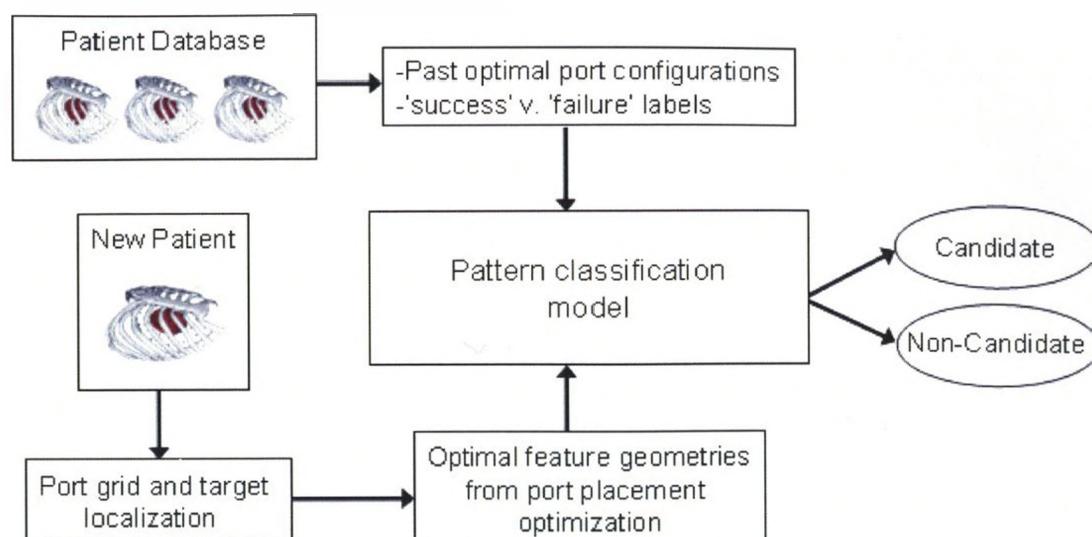


Figure 2.4 – General pattern classification scheme

in features associated with '*successful*' and '*failed*' MIRCAB cases is expected, and thus either parametric or non-parametric models can be used to statistically summarize the features of each class. Given a database of geometric features from past '*successful*' and '*failed*' cases, the models can be trained to expect certain values for a given class, and a decision can be computed.

As a basic illustration, suppose the classifier is to predict MIRCAB outcomes based on only one feature: distance of the left tool to the LAD blockage site. Two probability density functions, one for each patient class, profiling the measured feature can be constructed, and a vertical line can be imposed as a decision boundary (Figure 2.5) at some critical feature value. If small port-to-target distances were associated with '*failures*', then the decision rule would suggest that port-to-target feature measurements above the critical value would be MIRCAB '*candidates*', and feature measurement below the critical value would be '*non-candidates*'. Similarly, if a two-dimensional feature space were used for classification (e.g. port-to-target distances of both the left and right tools to the LAD), a decision boundary could be imposed, and so-forth for a d-dimensional feature classifier.

Critical to this process is: what features are used; and, how the decision boundary is calculated. Too many features can be redundant and add complexity to the model. And

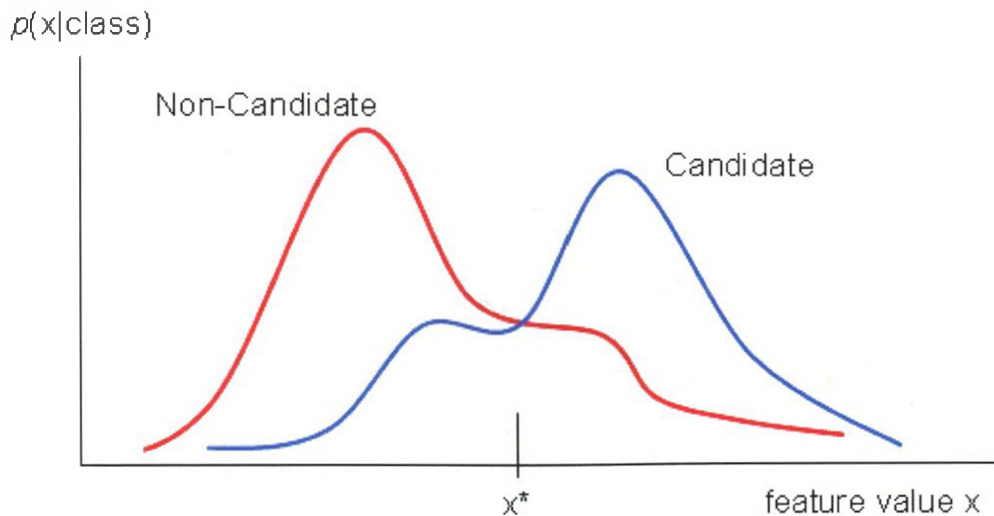


Figure 2.5 – Density functions of a single feature. Example probability density functions of a measured feature for each of two classes. Classification based on a critical value x^* leads to some errors since cases of both classes exist on either side. Note the profiled density functions shown above are arbitrary, but must integrate to 1.

generalized models have to be accepted to represent the feature spaces. When modeling the feature spaces probabilistically, the most important factor affecting the classifier results is the method for estimating the density of features associated with a particular class. The following section presents a Bayesian classification approach where the probability densities of features for each class are assumed to be Gaussian. This serves to set-up and define the basic classification problem. In Chapter 3, these methods are tested on patient data, methodologies for non-parametric classification (Parzen windowing and nearest neighbour approaches) are discussed, and results of the classifier models are compared by examination of classification error rates. What follows here is a formal definition [34] for statistical patient candidacy classification.

2.2.3.2. State of nature: a-priori probabilities

In a database of MIRCAB cases, each patient is assigned a state of nature, ω . For the patient candidacy problem, let $\omega = \omega_1$ for ‘successful’ cases, and $\omega = \omega_2$ for ‘failed’ cases. Given only a total count on ‘successful’ and ‘failed’ cases, a-priori probabilities can be assigned to reflect how likely each class is to appear: $P(\omega_1)$ is the probability of a *successful* case, and $P(\omega_2)$ is the probability of a *failed* case, where $P(\omega_1) + P(\omega_2) = 1$.

2.2.3.3. Class-conditional probabilities

For image-based classification, measured geometric features for each class are represented probabilistically. A single feature, x , is considered as a continuous random variable whose distribution depends on the state of nature, ω , and is expressed as $p(x|\omega)$. This class-conditional probability density function represents the probability of measuring x given the subject is of class ω , such that $p(x|\omega_1)$ and $p(x|\omega_2)$ describe the measured features of *successful* and *failed* cases respectively.

2.2.3.4. Bayes' decision rule

Given a database of past MIRCAB patients and their measured geometric features, both the a-priori probabilities $P(\omega_j)$ and the class-conditional densities $p(x|\omega_j)$ are known for $j = 1, 2$. Suppose that an incoming patient image dataset provides a measured feature x , how does this enable prediction of the state of nature, ω , or classification, of the patient? The joint probability of being class ω_j AND having feature measurement x is written as:

$$p(\omega_j, x) = P(\omega_j | x)p(x) = p(x | \omega_j)P(\omega_j) \quad (2.6)$$

Rearranging yields Bayes' formula:

$$P(\omega_j | x) = \frac{p(x | \omega_j)P(\omega_j)}{p(x)}, \quad (2.7)$$

where for the two-class case:

$$p(x) = \sum_{j=1}^2 p(x | \omega_j)P(\omega_j). \quad (2.8)$$

Bayes' formula enables conversion of the prior probabilities $P(\omega_j)$ to posterior probabilities $P(\omega_j|x)$: the probability of the patient class being ω_j given a measured value for feature x . Figure 2.6 shows how the patient can now be classified by following the Bayesian decision rule:

If $P(\omega_1|x) > P(\omega_2|x)$, classify as '*candidate*';

If $P(\omega_2|x) > P(\omega_1|x)$, classify as '*non-candidate*'.

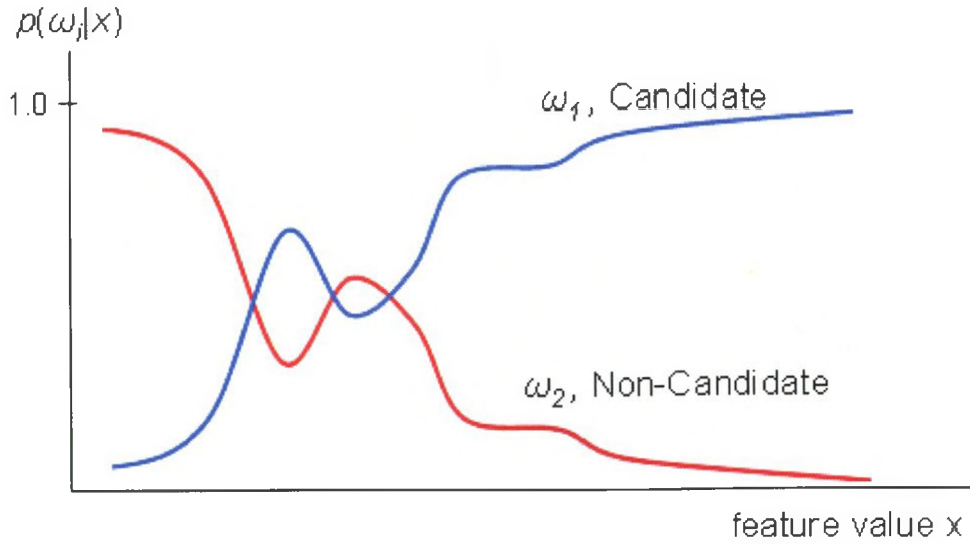


Figure 2.6 – Example posterior probabilities for Bayes' decision rule. After measuring a feature value x , classification for minimum error is based on which posterior probability is greater. Note the sum of the posteriors at all feature values is 1.

2.2.3.5. Bayesian risk with multiple features

To generalize the Bayesian decision rules to account for multiple features, a d -dimensional feature space yields a d -component feature vector \mathbf{x} . In addition, let $\lambda(\alpha_i | \omega_j)$ be introduced as a *loss function* representing the cost of taking the action α_i (deciding *candidate* for $i = 1$, and *non-candidate* for $i = 2$) given the true class of the patient ω_j . Letting $p(\mathbf{x} | \omega_j)$ be the class-conditional probability for \mathbf{x} , and given the prior probabilities, Bayes' formula is written as:

$$P(\omega_j | \mathbf{x}) = \frac{p(\mathbf{x} | \omega_j)P(\omega_j)}{p(\mathbf{x})}, \quad (2.9)$$

where

$$p(\mathbf{x}) = \sum_{j=1}^2 p(\mathbf{x} | \omega_j)P(\omega_j). \quad (2.10)$$

After measuring the feature vector \mathbf{x} for a particular patient, the loss function can be used to assess the cost of taking the action α_i . If the true class of the patient is ω_j , a loss $\lambda(\alpha_i | \omega_j)$ will be incurred. The posterior probability that the patient is of class ω_j is $P(\omega_j | \mathbf{x})$, and thus to minimize the expected loss for taking action α_i , compute:

$$R(\alpha_i | \mathbf{x}) = \sum_{j=1}^2 \lambda(\alpha_i | \omega_j) P(\omega_j | \mathbf{x}) \quad (2.11)$$

where $R(\alpha_i | \mathbf{x})$ is the conditional risk representing the expected loss for deciding 'candidate' ($i = 1$) or 'non-candidate' ($i = 2$) given \mathbf{x} . Bayes' decision rule is now based on minimizing the expected risk: action α_i should be taken for whichever $R(\alpha_i | \mathbf{x})$, $i = 1$ or $i = 2$, is lowest.

2.2.3.6. Two-category risk-based classification

In the proposed classification scheme, action α_1 corresponds to deciding the patient is of class ω_1 ('candidate') and action α_2 corresponds to deciding the patient is of class ω_2 ('non-candidate'). Simplifying the loss function notation as $\lambda_{ij} = \lambda(\alpha_i | \omega_j)$, the conditional risk can be rewritten explicitly for each classification action as:

$$R(\alpha_1 | \mathbf{x}) = \lambda_{11} P(\omega_1 | \mathbf{x}) + \lambda_{12} P(\omega_2 | \mathbf{x}) \quad (2.12a)$$

$$R(\alpha_2 | \mathbf{x}) = \lambda_{21} P(\omega_1 | \mathbf{x}) + \lambda_{22} P(\omega_2 | \mathbf{x}) \quad (2.12b)$$

In terms of posterior probabilities, the decision rule, decide ω_1 if $R(\alpha_1 | \mathbf{x}) < R(\alpha_2 | \mathbf{x})$, can be rewritten as:

If $(\lambda_{21} - \lambda_{11})P(\omega_1 | \mathbf{x}) > (\lambda_{12} - \lambda_{22})P(\omega_2 | \mathbf{x})$, decide ω_1 ('candidate');

Else, decide ω_2 ('non-candidate').

2.2.3.7. Minimum error rate classification

For a classification action α_i , and the true class of the patient ω_j , the classification decision is correct for $i = j$, and is incorrect otherwise. To avoid classification errors the decision rule should minimize the probability of error by assigning a zero-one loss function:

$$\lambda(\alpha_i | \omega_j) = \begin{cases} 0 & i = j \\ 1 & i \neq j \end{cases} \quad \text{for } i, j = 1, 2. \quad (2.13)$$

No loss is assigned to a correct classification, and unity loss is assigned to a misclassification. Here, the loss for a patient who could receive MIRCAB, but is classified as 'non-candidate' and recommended for open-chest CABG, is considered equal to the loss for a patient who should not receive MIRCAB, but is classified as

candidate and recommended for MIRCAB. This is justified, as the morbidity associated with conversion is equal to that of open-chest surgery itself. Designing weighted loss metrics for misclassification based on true incurred costs (normalizing monetary factors of treating the patients in hospital along with the quality of life of the patient post surgery) is beyond the scope of this classification routine. The expected conditional risk is then:

$$\begin{aligned}
 R(\alpha_i | \mathbf{x}) &= \sum_{j=1}^2 \lambda(\alpha_i | \omega_j) P(\omega_j | \mathbf{x}) \\
 &= \sum_{j \neq i} P(\omega_j | \mathbf{x}) \\
 &= 1 - P(\omega_i | \mathbf{x}),
 \end{aligned} \tag{2.14}$$

where $P(\omega_i | \mathbf{x})$ is the probability that classification action α_i is correct. To minimize classification error, the Bayesian decision rule needs to maximize the posterior probability, and the decision rule reduces to:

If $P(\omega_1 | \mathbf{x}) > P(\omega_2 | \mathbf{x})$, classify as '*candidate*';
 If $P(\omega_2 | \mathbf{x}) > P(\omega_1 | \mathbf{x})$, classify as '*non-candidate*'.

2.2.3.8. Discriminant functions and decision boundaries

In two-category classification, it is common to define a discriminant function to form the decision rule. Defining the discriminant function $g_i(\mathbf{x})$ for each class ($i=1,2$), the decision rule will divide the feature space into two regions \mathcal{R}_i . If $g_1(\mathbf{x}) > g_2(\mathbf{x})$, then \mathbf{x} is classified into region \mathcal{R}_1 , and \mathbf{x} is assigned class ω_1 , '*candidate*'. Similarly, if $g_2(\mathbf{x}) > g_1(\mathbf{x})$, then \mathbf{x} is classified into region \mathcal{R}_2 , and \mathbf{x} is assigned class ω_2 , '*non-candidate*'. The two regions are separated by the decision boundary where the discriminant functions are equal. To discriminate classes given a measured feature vector, the discriminant function is defined as:

$$g_i(\mathbf{x}) = P(\omega_i | \mathbf{x}) = p(\mathbf{x} | \omega_i) P(\omega_i) \tag{2.15}$$

The next section expresses features and classes as normal density functions, and is simplified when taking the natural logarithm of both sides to yield a new discriminant function:

$$g_i(\mathbf{x}) = \ln p(\mathbf{x} | \omega_i) + \ln P(\omega_i) \quad (2.16)$$

2.2.3.9. The normal density

The conditional densities $p(\mathbf{x} | \omega_i)$ and the prior probabilities $P(\omega_i)$ determine the classification routine. Assuming the features are normally distributed, the univariate feature density is:

$$p(x) = \frac{1}{\sqrt{2\pi}\sigma} \exp\left[-\frac{1}{2}\left(\frac{x-\mu}{\sigma}\right)^2\right], \quad (2.17)$$

where μ and σ are the mean and standard deviation for the feature x . Generalizing for a d -dimensional feature space:

$$p(\mathbf{x}) = \frac{1}{(2\pi)^{d/2} |\Sigma|^{1/2}} \exp\left[-\frac{1}{2}(\mathbf{x}-\boldsymbol{\mu})' \Sigma^{-1} (\mathbf{x}-\boldsymbol{\mu})\right], \quad (2.18)$$

where \mathbf{x} and $\boldsymbol{\mu}$ are the d -component mean vector, and d -by- d covariance matrix, $|\Sigma|$ and Σ^{-1} are the determinant and inverse of the covariance matrix, and t denotes matrix transposition.

2.2.3.10. Normal density discriminant functions

Substituting the multivariate normal density expressions into the two-class discriminant function $g_i(\mathbf{x}) = \ln p(\mathbf{x} | \omega_i) + \ln P(\omega_i)$, and assuming normal class-conditional distributions $p(\mathbf{x} | \omega_i) \sim N(\boldsymbol{\mu}_i, \Sigma_i)$, yields:

$$g_i(\mathbf{x}) = -\frac{1}{2}(\mathbf{x}-\boldsymbol{\mu}_i)' \Sigma_i^{-1} (\mathbf{x}-\boldsymbol{\mu}_i) - \frac{d}{2} \ln 2\pi - \frac{1}{2} \ln |\Sigma_i| + \ln P(\omega_i). \quad (2.19)$$

Since the $\frac{d}{2} \ln 2\pi$ term is independent of class, it can be dropped, and the discriminant function can be rewritten as a quadratic:

$$g_i(\mathbf{x}) = \mathbf{x}' \mathbf{W}_i \mathbf{x} + \mathbf{w}_i' \mathbf{x} + w_{i0}, \quad (2.20)$$

where

$$\mathbf{W}_i = -\frac{1}{2} \Sigma_i^{-1},$$

$$\mathbf{w}_i = \Sigma_i^{-1} \boldsymbol{\mu}_i,$$

and,

$$w_{i0} = -\frac{1}{2} \boldsymbol{\mu}_i' \boldsymbol{\Sigma}_i^{-1} \boldsymbol{\mu}_i - \frac{1}{2} \ln |\boldsymbol{\Sigma}_i| + \ln P(\omega_i). \quad (2.21)$$

Figure 2.7 and 2.8 illustrate two-category classification decision regions formed by univariate (single-featured) and bivariate (two-featured) normal distributions. The choice of features used for classifications has implications on the model complexity, and should be reduced as much as possible to ease computation [34]. Chapter 3 expands on feature selection given a database of class conditional feature densities.

2.3. Intra-operative guidance

After optimizing the port positions and classifying candidacy for an incoming MIRCAB patient, surgeons must accurately transfer port placement plans onto the patient's chest in the operating room. This intra-operative mapping is implemented by two joint procedures: 1) registration of the image data coordinates to real-world coordinates recorded by optical tracking; and, 2) superposition of the port positions directly onto the patient's chest using optically-guided laser projection.

2.3.1. Registration

Paired-point rigid-body registration techniques [35,36] are used to align the image data coordinate frame to the world coordinate frame. This methodology requires that a set of (at least three) points be identifiable by both coordinate systems. Fiducial markers which are visible in CT, and whose positions can be measured by an optical tracking system are used as the common points. These landmarks are placed strategically on the patient's chest over structures whose positions are relatively rigid (detailed selection of landmark sites is discussed in Chapter 4). Despite efforts to choose rigid landmarks, the landmark locations often move relative to each other from when the patient is imaged to when they are on the OR table. Changes in relative landmark positioning are due to chest insufflation and deflation of the left lung (changing the chest size) and anaesthesia (allowing the arms to hang limp during surgery). Implications of the registration error incurred from this problem are discussed in Chapter 4.

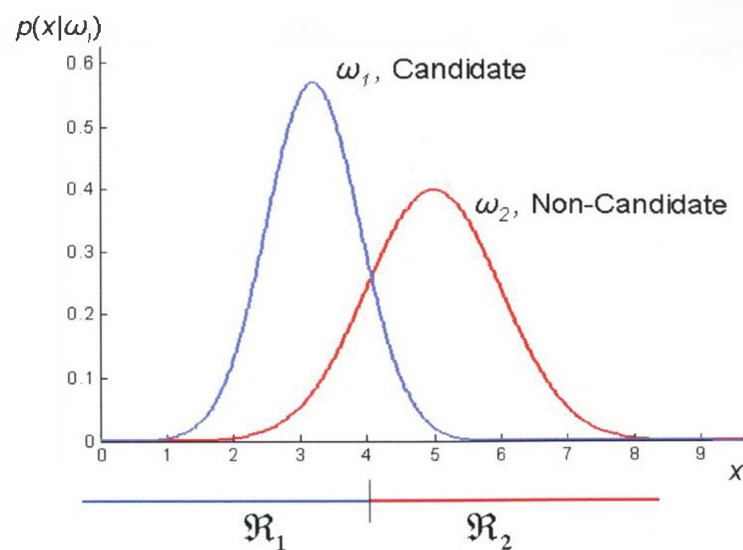


Figure 2.7 – Two-class decision regions for 1D normal distributions. The decision boundary between classification regions shifts based on the posterior and prior probabilities.

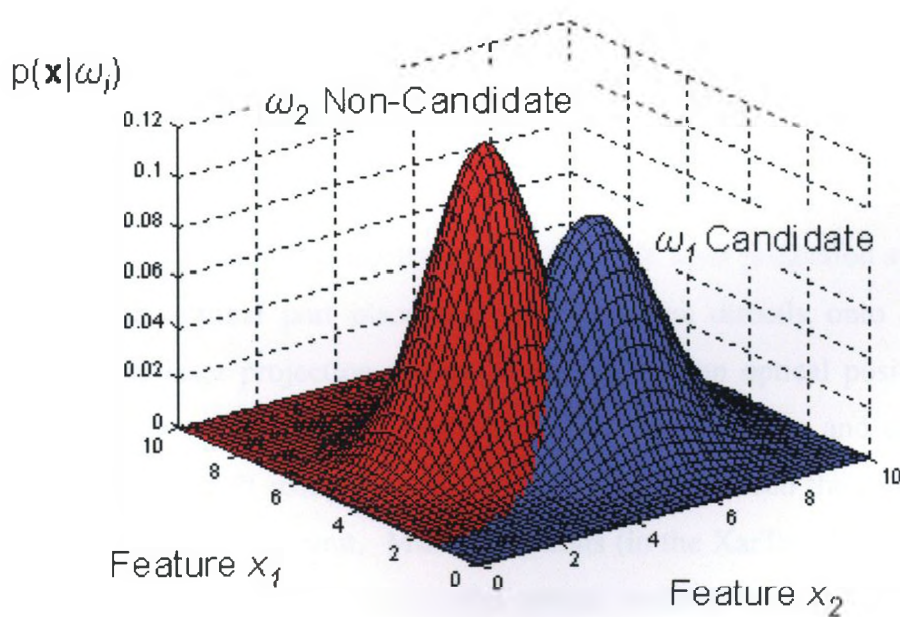


Figure 2.8 – Two-class decision regions for 2D normal distributions.

The image-coordinate landmarks, located manually in the Atamai viewing software, are represented as:

$$\mathbf{x}_{ILM} = \begin{bmatrix} x_{ILM,1} & y_{ILM,1} & z_{ILM,1} \\ \vdots & \vdots & \vdots \\ x_{ILM,N} & y_{ILM,N} & z_{ILM,N} \end{bmatrix},$$

where $\mathbf{x}_{ILM,i}$ represents the image coordinates of the i^{th} landmark for $i = 1 \dots N$.

Similarly, the real-world landmarks, located by optical tracking, are represented as:

$$\mathbf{x}_{WLM} = \begin{bmatrix} x_{WLM,1} & y_{WLM,1} & z_{WLM,1} \\ \vdots & \vdots & \vdots \\ x_{WLM,N} & y_{WLM,N} & z_{WLM,N} \end{bmatrix},$$

where $\mathbf{x}_{WLM,i}$ represents the measured world coordinates of the i^{th} landmark for $i = 1 \dots N$.

A registration transformation [35, 36] including a rotation matrix, \mathbf{R} , a translation vector, \mathbf{T} , and a scaling factor, a , is then sought to align the coordinate systems by satisfying with minimal error:

$$\mathbf{x}_{WLM} = a\mathbf{R}\mathbf{x}_{ILM} + \mathbf{T}. \quad (2.22)$$

2.3.2. Laser projection

The commercially available, optically guided XarTraX laser projection system [15] is used to display the optimal port placement configurations directly onto the patient's chest. The XarTraX laser projection system is mounted to an optical position tracking system (NDI, Waterloo, ON). A hardware unit (power, amplifiers, and controllers) is controlled by a custom API using RS-232 communication between the optical tracking system and the laser projection unit. Mirror positions (in the XarTraX) are controlled to direct an IR laser to positions recorded by the optical tracking system. The optimal port positions are computed in the image coordinate system, and are represented as:

$$\mathbf{P}_{\text{opt}} = [\mathbf{p}_L^{\text{opt}} \quad \mathbf{p}_E^{\text{opt}} \quad \mathbf{p}_R^{\text{opt}}]^t,$$

where the row entries are vectors specifying the optimal port coordinates for the left surgical tool, endoscope, and right surgical tool. Application of the image-to-world

registration transformation to the image coordinate optimal port configuration yields the world optimal port configuration to be used for optically guided laser projection:

$$\mathbf{P}_{W,opt} = \mathbf{aRP}_{opt} + \mathbf{T}.$$

The laser projections of the optimal port positions are then displayed in sequence to the coordinates in the optical tracking (real-world) frame. XarTraX projections are generally repeatable to within 1 mm.

2.3.3. Error assessment

The registration accuracy and port placement accuracy are assessed using established Fiducial Registration Error (FRE) and Target Registration Error (TRE) metrics [37]. The FRE describes the accrued error that can be attributed to: the tracking system used for registration, and human error in locating the fiducial markers both in the image and real-world coordinates. This registration error is defined by the root mean square error between the registered landmark world coordinates, $\hat{\mathbf{x}}_{WLM}$, and the measured landmark world coordinates:

$$FRE = \sqrt{\frac{1}{N} \sum_{i=1}^N \|\hat{\mathbf{x}}_{WLM,i} - \mathbf{x}_{WLM,i}\|^2}, \quad (2.23)$$

where $\hat{\mathbf{x}}_{WLM,i} = \mathbf{R}\mathbf{x}_{ILM,i} + \mathbf{T}$ for all $i = 1 \dots N$ fiducial landmarks, and

$$\|\hat{\mathbf{x}}_{WLM,i} - \mathbf{x}_{WLM,i}\| = \sqrt{(\hat{x}_{WLM,i} - x_{WLM,i})^2 + (\hat{y}_{WLM,i} - y_{WLM,i})^2 + (\hat{z}_{WLM,i} - z_{WLM,i})^2}. \quad (2.24)$$

Computation of the TRE requires that the projected port position be measured in the world coordinate system using optical tracking. The measured port positions are denoted as $\mathbf{P}_{m,opt} = [\mathbf{p}_L^m \quad \mathbf{p}_E^m \quad \mathbf{p}_R^m]^T$. The TRE is calculated as the root mean square error between the measured and optimal port positions in world coordinates, such that:

$$TRE = \sqrt{\frac{1}{3} \sum_{i \in (L,E,R)} \|\mathbf{p}_i^m - \mathbf{p}_i^{opt}\|^2}. \quad (2.25)$$

2.4. Post-operative database management

Finally, following surgery, the pre-operative optimization and classification databases are updated and re-trained based on the success of the intervention. All

optimal feature values are recomputed to include the newest patient's data. Only successful MIRCAB port configurations are used to train the port placement optimization features, while port configurations for both failed and successful cases are used to update the patient candidacy classification model. As more patients are added to the database, the optimization and classification routines become more representative of the patient population, enabling better port placement selections, and more accurate classification.

2.5. Summary of goals

Ultimately, the port placement optimization and patient candidacy classification routines will enable safe selection of patients and port positions for MIRCAB, reducing: surgical failures (conversion to open-chest surgery); morbidity for the patient; and, burden of care for the physicians and hospital. The following two chapters investigate port placement optimization and candidacy classification for a database of past MIRCAB patients. In addition, the use of a laser projection system for mapping port positions onto the patient in the OR, following registration, is evaluated. The laser projection system is first evaluated on a phantom test bed setup, and then on four patient case studies. Combined, the pre-operative planning and intra-operative guidance should improve the efficacy of MIRCAB as an effective accessible intervention.

Chapter 3. Pre-operative planning: Port placement optimization and patient candidacy classification

3.1. Pre-operative planning overview

This chapter details the experiments and results on port placement optimization and patient candidacy classification using a database of seventeen MIRCAB patients. Characteristics of the patient population including differences in imaging protocols and notable features of the patients related to surgical outcomes (revealed by expert radiologists and surgeons) are discussed to appreciate case-by-case variability. Feature geometries extracted from pre-operative CT patient images are summarized, and are first used to train and test the port placement optimization algorithm. Optimal port placement configurations are compared to the manual expert surgeon selected configurations to validate the routine. Second, the feature database is used to train and test various patient candidacy classification routines and the classification results are compared to the true past surgical outcomes.

3.2. Experiments: Optimal port placement

3.2.1. Pre-operative CT imaging

All subjects were imaged using 4-slice spiral CT (typically 120 kV, 1.5 mA, FOV = 45 cm, matrix = 256×256 , slice thickness = 1.125 mm, imaging time = 15.4 s, GE Medical Systems, Milwaukee, WI). Patient positioning was critical for achieving registration goals (Chapter 4). With patients imaged flat on their backs, but operated on while tilted on the OR table, the relative change in positioning of the fiducial markers would introduce error to the assumed rigid-body registration. For this reason, the imaging protocol was adjusted to position the patient the same way both for imaging and surgery. Imaging for all four laser projection port placement trials was performed in this manner. As well, all patients were imaged with one arm above their head, and the other relaxed by their side, to duplicate the patient pose during surgery.

3.2.2. The patient population

The participating patients ($N = 17$) in this study all consented to research approved by The University of Western Ontario research ethics board (Appendix A). Requiring CABG surgery to bypass single LAD blockage sites, each patient elected to undergo MIRCAB over conventional open-chest surgery. Table 3.1 summarizes variability among the patient cases including: gender, positioning for CT imaging (supine - flat on their back, or tilted on a bed sheet to replicate their position on the OR table), outcome of the surgery, and special notes (reasons for failed MIRCAB, critical intra-thoracic space geometry, and use of fiducial markers for registration and intra-operative laser projection port placement trials). Amongst these cases fourteen were eventually successful, and three were subject to conversion.

Table 3.1 – Patient population summary

Patient number	Gender (M / F)	Imaging position (Flat / Tilted)	Outcome (Success / Failure)	Special notes
1	F	Flat	FAILURE	First failed case, first CT (scanned post-operation)
2	F	Flat	SUCCESS	N/A
3	M	Flat	SUCCESS	
4	M	Tilted	SUCCESS	
5	M	Flat	SUCCESS	Minimal intra-thoracic space for surgical tool manipulation
6	M	Flat	FAILURE	Insufficient intra-thoracic space
7	F	Flat	FAILURE	
8	M	Flat	SUCCESS	N/A
9	M	Flat	SUCCESS	Pleural plaque forced re-insertion of a new port
10	M	Tilted	SUCCESS	Pilot trial testing laser projection for port placement
11	M	Tilted	SUCCESS	Pilot trial imaging with fiducial markers
12	M	Tilted	SUCCESS	First laser projection case
13	M	Tilted	SUCCESS	Second laser projection case
14	M	Flat	SUCCESS	Minimal intra-thoracic space
15	F	Tilted	SUCCESS	N/A
16	M	Tilted	SUCCESS	Third laser projection case
17	M	Tilted	SUCCESS	Fourth laser projection case

3.2.3. Extraction of patient feature geometry

All of the feature geometry extraction was performed retrospectively after both imaging and surgery across the patient image database (following the procedures outlined in Chapter section 2.2.2). First, the rib and skin surfaces were created to add 3D context for exploring the images. Second, the local expert surgeon indicated the sites of the manually chosen optimal port placement configurations used for surgery. Third, the coordinates of the three target sites (LAD blockage site, most superior end of the LITA, and most inferior end of the LITA) were marked. Finally, feature geometries (port-to-port distances, port-to-target distances at each target site, and angles between instruments at each target site) were computed for each patient. These feature measurements then form a database for use in port placement optimization and patient candidacy classification.

3.2.4. Port placement optimization

The port placement optimization routine (Chapter section 2.2.2.1 – 2.2.2.2) was implemented in MATLAB, and was evaluated using a ‘leave-one-out’ strategy. To optimize the port placement configurations for a single patient (as if they were a new incoming patient), and to test the optimization on each patient, the feature database was trained iteratively by removing one patient at a time from the database. That removed patient was then subject to the optimization routine. Only successful MIRCAB subjects were used in training the optimization algorithm. Figure 3.1 shows a flow chart of the ‘leave-one-out strategy’ for port placement optimization.

3.2.5. Optimization implementation and testing

For each removed patient, the optimal feature vector and upper/lower bounds were trained with the remainder of the patient database using the expert selected port configurations and target site locations. Then, for the patient at hand, a grid of potential port positions was manually selected along the intercostal spaces, and the three target locations were marked. From the grid of port locations, a complete list of potential port triad configurations was formed. A 3-dimensional search space (one dimension for each

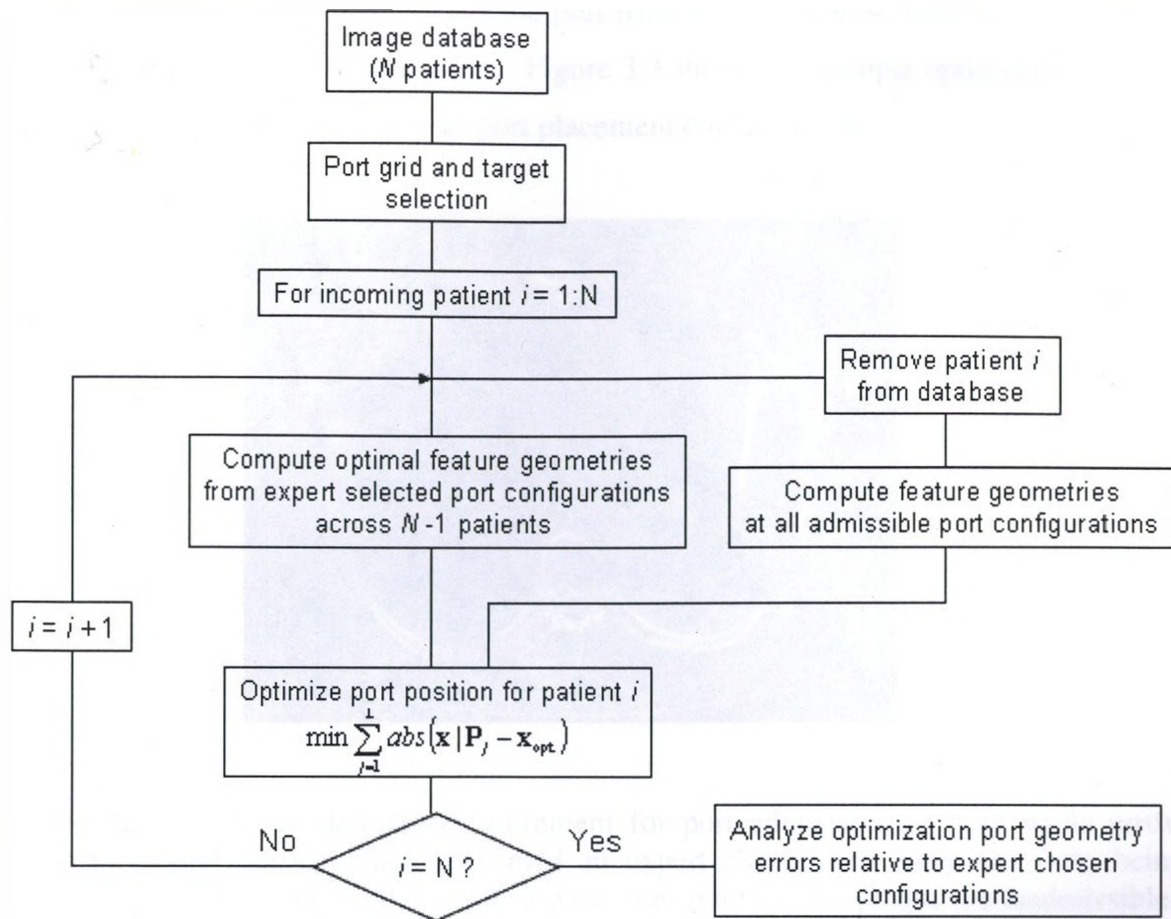


Figure 3.1 – Leave-one-out port placement optimization

of the three surgical tools) was set up such that each coordinate in the search domain corresponds to a unique port triad configuration. Prior to optimization, each potential port configuration was labelled as ‘admissible’ or ‘non-admissible’ according to the upper and lower feature bounds. In addition, ‘admissible’ port configurations were checked to have collision-free paths from all ports to all targets. Figure 3.2 shows the unique case of patient $N = 9$, where pleural plaque blocked the path of the surgical tools and required incision of a new port. Had collision-detection admissibility been evaluated at the time, this would have eliminated the need to re-insert a new port entry.

Finally, the optimization objective metric was evaluated exhaustively over all ‘admissible’ configurations in the search space to compute the cumulative error between the feature vector (evaluated at each potential port triad) and the optimal feature vector. A ranked list of ports triad scored by the error of their feature vector relative to the

optimal feature vector is formed, and the port triad with the lowest error is chosen as the optimal port placement configuration. Figure 3.3 shows an example optimization search space map used to select an optimal port placement configuration.

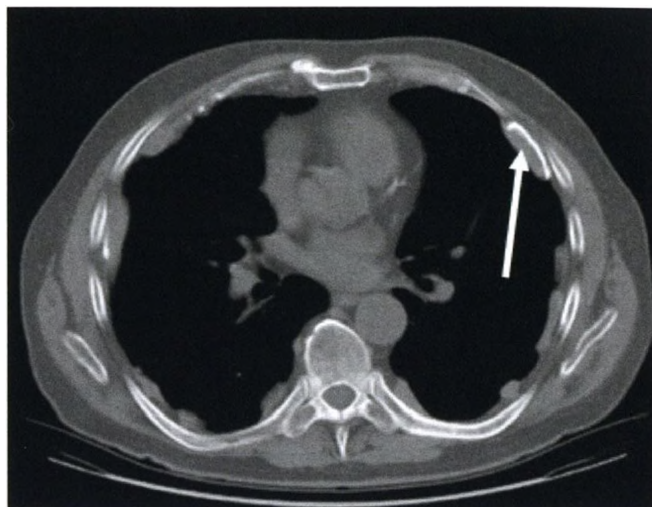


Figure 3.2 - Collision detection requirement for port admissibility. The white arrow points to pleural plaque which prevented an expert chosen-port entry site from being used. Ports whose vectors towards the surgical sites intersect the plaque are inadmissible.

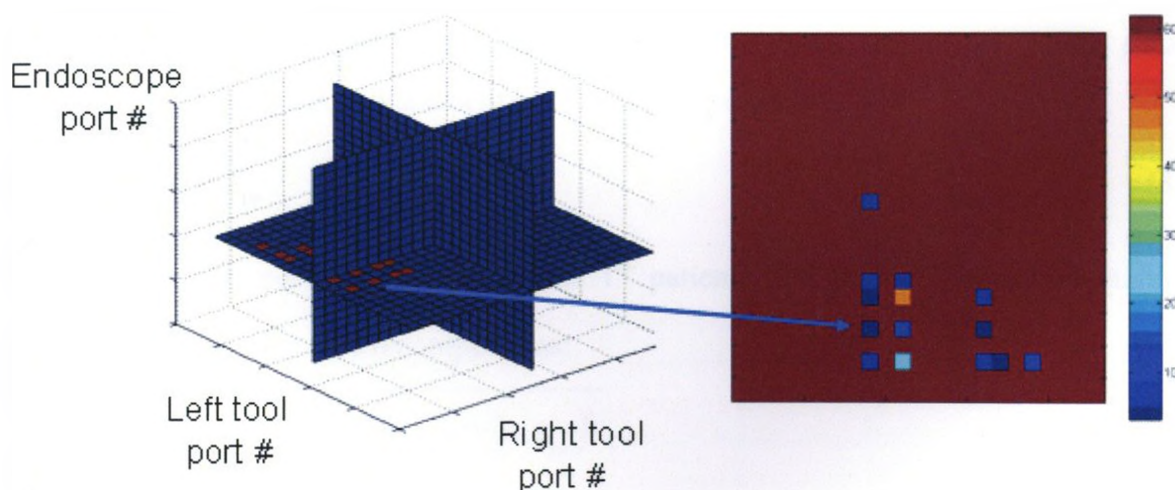


Figure 3.3 – Optimization search space. *Left:* Each possible port configuration from a grid of numbered port locations is noted as admissible (*red*) or inadmissible (*blue*). *Right:* The admissible ports are scored by the optimization objective metric to find the highest ranked (lowest error) port configuration (indicated by the blue arrow).

3.3. Results: Optimal port placement

The port placement optimization was computed for each patient after retraining the optimal feature vector on the remaining successful patient database. To validate the results of the optimization algorithm, each patient's computed optimal port configurations were compared to the port configurations manually chosen in the past by the expert surgeon. Port placement error between the computed and expert-chosen optimal port configurations was computed on a per-patient basis using the following root mean square metric:

$$e_{pp} = \sqrt{\frac{1}{3} \sum_{i \in (L,E,R)} \|\mathbf{p}_i^{\text{exp}} - \mathbf{p}_i^{\text{opt}}\|^2}, \quad (3.1)$$

where $\mathbf{p}_i^{\text{exp}}$ holds the coordinates of the three expert-selected ports, and $\mathbf{p}_i^{\text{opt}}$ holds the coordinates of the three computed optimal ports for a particular patient. The variability among port placement error at each port, on a per patient basis, is computed as the standard deviation between a single port's offset (between expert and computed optimization) and the above port placement error:

$$\sigma_{pp} = \sqrt{\frac{1}{3} \sum_{i \in (L,E,R)} (\|\mathbf{p}_i^{\text{exp}} - \mathbf{p}_i^{\text{opt}}\| - e_{pp})^2}. \quad (3.2)$$

To summarize the port placement optimization error across the entire patient database, the average port placement error was computed as:

$$\bar{e}_{pp} = \frac{1}{N} \sum_{i=1}^N e_{pp}^i, \quad (3.3)$$

where e_{pp}^i is the per-patient error of the i^{th} patient. The patient population standard deviation on the error was recomputed as:

$$\bar{\sigma}_{pp} = \sqrt{\frac{1}{3N} \sum_{j=1}^N \sum_{i \in (L,E,R)} (\|\mathbf{p}_{i,j}^{\text{exp}} - \mathbf{p}_{i,j}^{\text{opt}}\| - \bar{e}_{pp})^2}, \quad (3.4)$$

where the subscript j iterates over all N patients. Figure 3.4 shows an example image with computed and expert-selected optimal port configurations. The per-patient and population-wide error analyses are summarized in Table 3.2. Note the outlier data of patient 13: computed optimal ports did not match the expert selections as well as for the remaining patients. Regardless, the computed geometry still appeared acceptable.

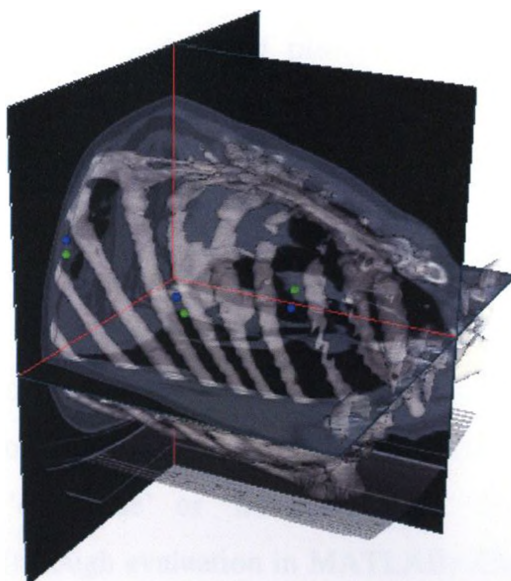


Figure 3.4 – Computed vs. expert selected optimal port placement. Computer optimized ports (*green spheres*) are very representative of expert manually selected ports (*blue spheres*). The distance between each port pair is used to assess error in the optimization algorithm.

Table 3.2 - Port placement optimization error summary

Patient Number (successes only)	e_{pp} (mm)	σ_{pp} (mm)
<i>Per-patient error</i>		
2	15.7	6.2
3	9.3	4.3
4	12.2	4.7
5	12.7	3.3
8	11.5	5.4
9	8.2	3.9
10	11.9	4.6
11	18.7	6.9
12	12.6	4.4
13	25.7	17.7
14	15.9	6.6
15	7.4	4.2
16	16.1	7.8
17	14.2	5.2
<i>Population-wide error</i>		
$N=14$	$\bar{e}_{pp} = 13.7$ mm	$\bar{\sigma}_{pp} = 5.1$ mm

3.4. Experiments: Patient candidacy classification

While it is possible to optimize port placement for any incoming patient, some patients should not undergo MIRCAB due to small intra-thoracic space, and should be referred to open-chest CABG. For this reason it is necessary to evaluate patient candidacy for robotic intervention. Candidacy assessment has never been addressed in any current port placement methods [2,3,5,6,7,12,38,39]. Accurate prediction of candidacy will reduce the occurrence of failed MIRCAB cases requiring conversion. Detailed here are the experiments for patient candidacy classification routines used to recognize patterns among ‘successful’ and ‘failed’ MIRCAB cases and to identify incoming patients as ‘candidate’ or ‘non-candidate’. Three different classification methods are compared (through evaluation in MATLAB): Gaussian, Parzen window, and nearest neighbour classification. These three methods contrast the assumptions on whether the patient feature geometries follow probabilistic (Gaussian, Parzen), parametric (Gaussian), or non-parametric (Parzen, nearest neighbour) models. The models are each used to classify patients retrospectively, again using the ‘leave-one-out’ strategy. The classification routines presented below are considered to be supervised learning techniques in which the true outcome of all the training cases is known. Figure 3.5 shows a flow diagram indicating the general routine for candidacy classification.

3.4.1. Reduction of important feature geometries

Choosing a subset of features upon which to base classification is critical. Firstly, the chosen features should be directly related to the causes of MIRCAB failure. Second, too many features add dimensionality and complexity to the models, and in many cases [34], can prevent evaluation of the algorithms (e.g. if features are, unknowingly, approximate linear combinations of each other, then the feature matrix is singular and cannot undergo required inversions).

From a database of patient features, where each past patient has been labelled as ‘success’ or ‘failure’, a class-conditional probability density function, $p(\mathbf{x} | \omega_i)$, profiling the feature vector is formed as described throughout Chapter sections 2.2.3.1 – 2.2.3.6. Figure 3.6 shows the class-conditional probability density functions of each feature of a

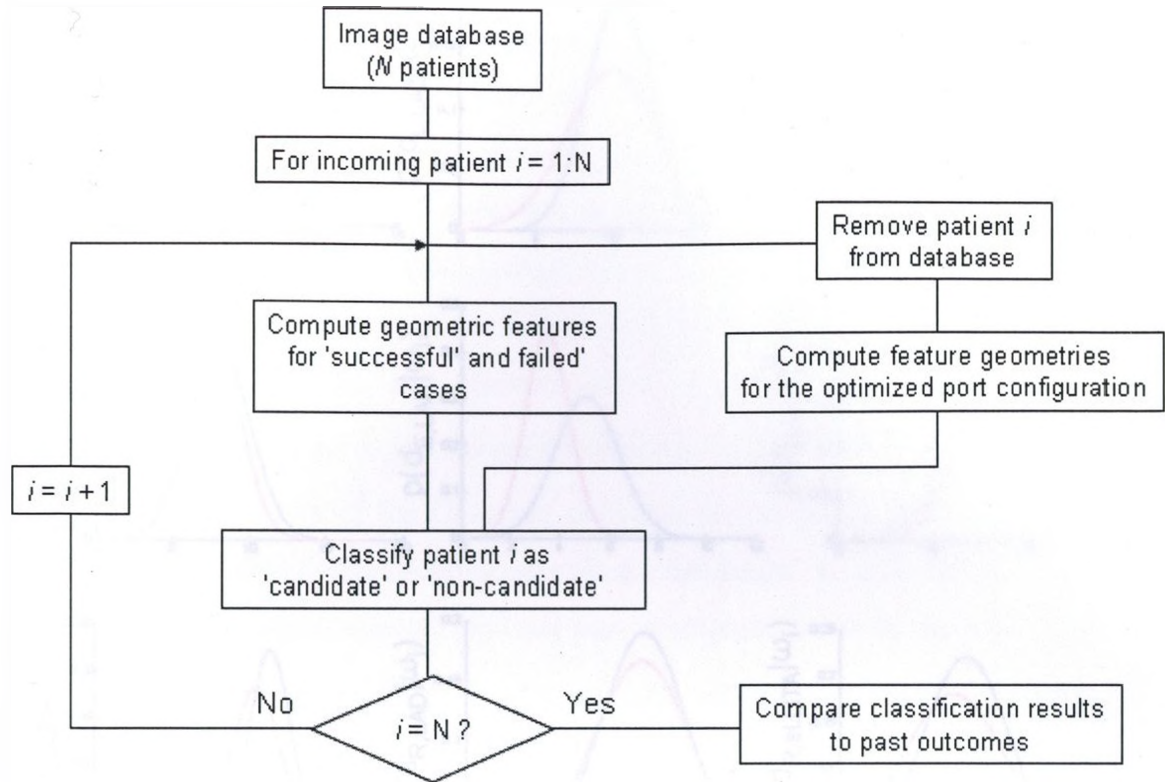


Figure 3.5 – Leave-one-out flow diagram for patient candidacy classification

reduced feature set of on its own. Here, using univariate normal distribution estimations eliminates dimensional complexity when inspecting for which features vary the most between ‘success’ and ‘failure’ classes. More advanced feature selection methods exist, such as unsupervised clustering algorithms [34], but are beyond the scope of the present implementation. In addition to inspection of the class-conditional feature densities, practical interpretation of which geometries relate to small intra-thoracic space (the main reason for MIRCAB failure) allows assignment of a reduced feature vector for patient candidacy classification:

$$\mathbf{x} = [d_{L,LAD}, d_{L,iLITA}, d_{L,sLITA}, d_{R,LAD}, d_{R,iLITA}, d_{R,sLITA}, d_{E,LAD}, d_{E,iLITA}, d_{E,sLITA}].$$

Note that the reduced feature vector contains only the port-to-target distances at each target site. Port-to-port distances are not required because they are independent of the shape of the thoracic cavity, and angles between instruments are not required as their computation is a function of the port-to-port and port-to-target geometries.

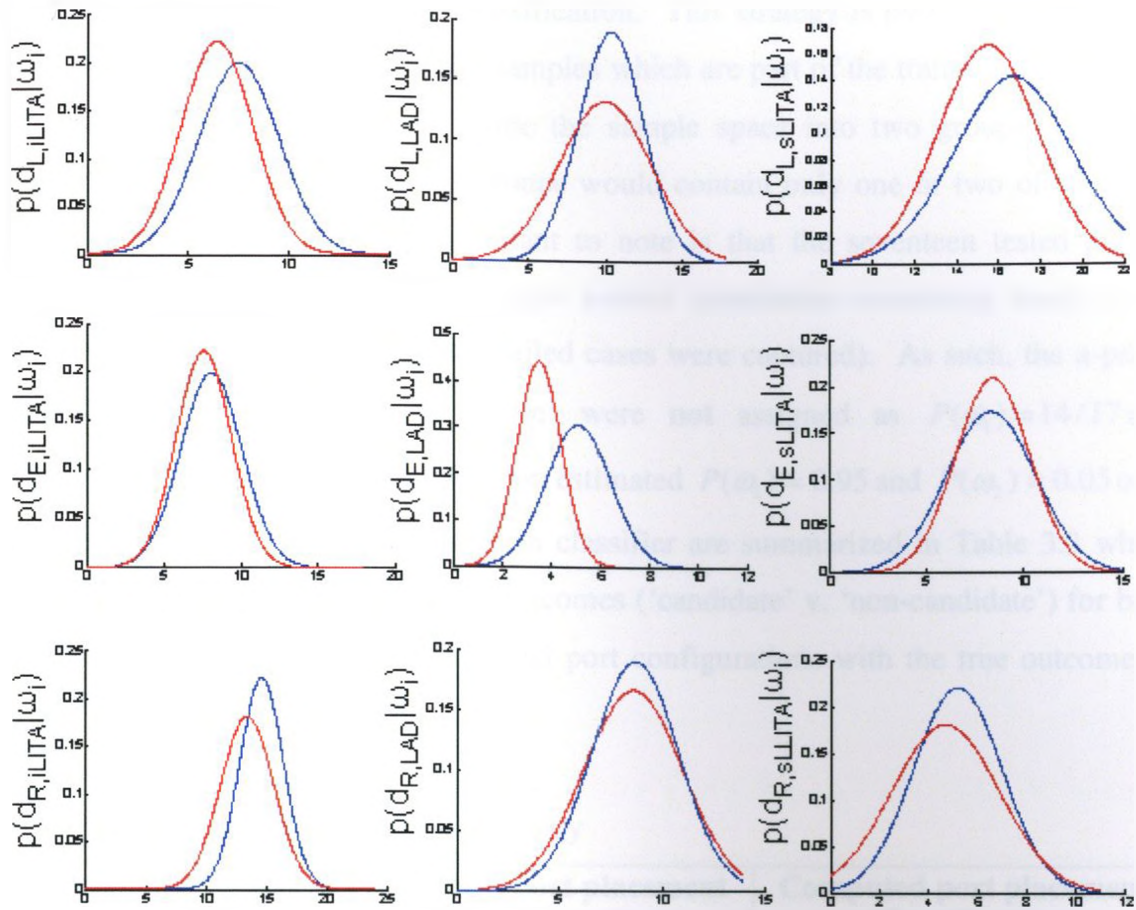


Figure 3.6 – Gaussian class-conditional feature densities. Candidate features (*blue*) and non-candidate features (*red*) are not obviously different, but when combined in a multi-dimensional feature vector, can be classified. The most apparent distinguishing feature is the port-to-target distance from the endoscope port to the LAD (*middle*).

3.5. Results: Patient candidacy classification

3.5.1. Gaussian candidacy classification

Gaussian classification requires knowledge of the class-conditional feature densities and of the a-priori probabilities of each class: this combination enables switching the conditionality statement, using Bayes' Theorem, to express $p(\omega_i | \mathbf{x})$, the posterior probability of a new patient belonging to either class given the measured feature vector. The classification is then performed to identify the patient as 'candidate' or 'non-candidate' following the methodology in Chapter sections 2.2.3.2 - 2.2.3.10.

Using the 'leave-one-out' strategy, the Gaussian classifier model is retrained, based on the 9-dimensional reduced feature vector, with patients removed one at a time. The

removed patient is then subject to classification. This strategy is used due to the small sample size: it is inappropriate to test samples which are part of the training set [34], and there are insufficient subjects to divide the sample space into two groups – one for training and one for testing (as the groups would contain only one or two of the three available ‘failed’ cases). Also important to note is that the seventeen tested patient samples are a subset of a much larger patient population containing many more successful MIRCAB cases (all of the failed cases were captured). As such, the a-priori probabilities for ‘success’ and ‘failure’ were **not** assigned as $P(\omega_1) = 14/17$ and $P(\omega_2) = 3/17$. Rather, the expert surgeon estimated $P(\omega_1) = 0.95$ and $P(\omega_2) = 0.05$ over all patients. The results of the Gaussian classifier are summarized in Table 3.3 which compares the candidacy classification outcomes (‘candidate’ v. ‘non-candidate’) for both the computed and expert-selected optimal port configurations with the true outcome of the past cases (‘success’ v. ‘failure’).

Table 3.3 – Gaussian classification summary

Patient Number	Observed outcome	Expert port placement classification	Computed port placement Classification
1	FAILURE	NON-CANDIDATE	NON-CANDIDATE
2	SUCCESS	CANDIDATE	CANDIDATE
3	SUCCESS	CANDIDATE	CANDIDATE
4	SUCCESS	CANDIDATE	CANDIDATE
5	SUCCESS	CANDIDATE	CANDIDATE
6	FAILURE	CANDIDATE	NON-CANDIDATE
7	FAILURE	NON-CANDIDATE	NON-CANDIDATE
8	SUCCESS	CANDIDATE	CANDIDATE
9	SUCCESS	CANDIDATE	CANDIDATE
10	SUCCESS	CANDIDATE	CANDIDATE
11	SUCCESS	CANDIDATE	NON-CANDIDATE
12	SUCCESS	NON-CANDIDATE	CANDIDATE
13	SUCCESS	CANDIDATE	CANDIDATE
14	SUCCESS	CANDIDATE	CANDIDATE
15	SUCCESS	CANDIDATE	CANDIDATE
16	SUCCESS	CANDIDATE	CANDIDATE
17	SUCCESS	CANDIDATE	CANDIDATE
N = 17		15/17 correct *1 miss, 1 false alarm	16/17 correct 1 false alarm

* Note the classification is trying to detect the low-probability ‘failure’. An incoming ‘candidate’ classified as a ‘non-candidate’ is a ‘false alarm’, and an incoming ‘non-candidate’ classified as a ‘candidate’ is a ‘miss’.

3.5.2. Parzen window candidacy classification

The former Gaussian classification method assumes that the form of the underlying probability density function describing the feature vector is known. Such parametric techniques presume that the feature densities are unimodal. This section presents a non-parametric probabilistic classification approach that allows arbitrary multimodal distributions to override assumptions made about the underlying feature densities. Here, Parzen window estimation of the feature densities $p(\mathbf{x} | \omega_i)$ is used before applying Bayes' Theorem to compute decision boundaries according to the posterior probabilities $p(\omega_i | \mathbf{x})$.

The Parzen window approach [29] defines the class-conditional feature densities as an average of normal densities centred at each of the features samples:

$$p(\mathbf{x} | \omega_i) = \frac{1}{N} \sum_{j=1}^N \frac{1}{h_N} \varphi\left(\frac{\mathbf{x} - \mathbf{x}_j}{h_N}\right), \quad (3.5)$$

where \mathbf{x}_j is the j^{th} sample of the feature vector \mathbf{x} and $h_N = h_1 / \sqrt{N}$, with h_1 being an adjustable window width parameter. The window function is chosen as a zero-mean, unit-variance, and multivariate normal density of the form:

$$\varphi(\mathbf{u}) = \frac{1}{\sqrt{2\pi}} e^{-u^2/2}. \quad (3.6)$$

To illustrate the behaviour of the density estimation for features belonging to a single class, Figure 3.7 profiles example Parzen window estimates of a single featured (univariate) normal density while varying the parameter h_1 . In order to find the decision boundaries for classification, the class-conditional densities are estimated for each class, and then the test samples are labelled according to computed posterior probabilities.

The supervised learning 'leave-one-out' strategy was used again to test the Parzen window classification on the MIRCAB patient database (with the 9-dimensional reduced feature vector). Both computed and expert-selected optimal port configurations were tested. Table 3.4 summarizes the classification results for computer optimal port configurations and shows how varying the window width parameter effects classification accuracy.

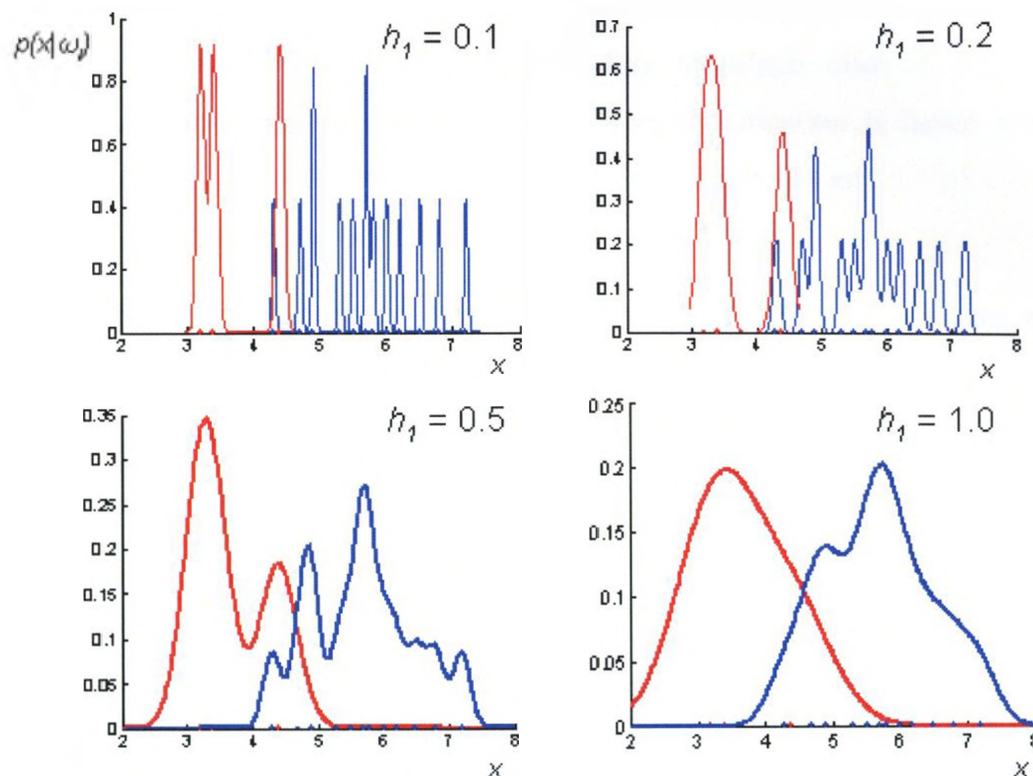


Figure 3.7 - Parzen window density estimation for one feature. Candidate (*blue*) and non-candidate (*red*) Parzen window densities of an example feature (endoscope to LAD port-to-target distance). Single measurements which form the densities are shown as points on the x -axis. Note as window parameter h_1 is lower, the densities approach an impulse at each sample point, whereas when h_1 is, the densities approach a Gaussian.

Table 3.4 – Parzen window classification summary

Parameter h_1	0.1	0.2	0.5	1.0	10
Classification results	15/17 1 miss, 1 false alarm	16/17 1 miss	17/17	16/17 1 miss	16/17 1 false alarm

3.5.3. Nearest-neighbour candidacy classification

The final classification method tested was nearest neighbour estimation. This non-parametric approach bypasses probabilistic density estimation of the class-conditional features $p(\mathbf{x} | \omega_i)$, and aims to directly compute classification decision boundaries based on the posterior probabilities $p(\omega_i | \mathbf{x})$. Given a set of training features, an incoming sample feature vector, \mathbf{x} , is classified by growing a decision boundary cell outward from

that sample until it encloses k neighbouring samples: the k -nearest-neighbours of \mathbf{x} . The k -nearest-neighbour rule classifies \mathbf{x} according to which class is most frequently represented among the k nearest samples. The classification is hence based on the posterior probabilities estimated among the nearest neighbours as:

$$P(\omega_m | \mathbf{x}) = \max_i P(\omega_i | \mathbf{x}). \quad (3.7)$$

The assigned classification ω_m takes the label of whichever class has the majority of samples among the k nearest samples (and hence, even numbers for k should be avoided). An equivalent implementation of this method is to evaluate a distance metric from the sample features \mathbf{x} to all training samples \mathbf{x}' :

$$d_{kNN} = \sum_{j=1}^M \sum_{i=1}^N \|\mathbf{x}_j - \mathbf{x}'_{i,j}\|, \quad (3.8)$$

where the inner summation iterates over the N patients, and the outer summation sums over the M features. Searching for the k lowest distance metric evaluations then forms a ranked list of the k training samples that fall closest to \mathbf{x} . The classification for \mathbf{x} is assigned based on what class takes the majority of the k nearest neighbours.

Again, the 'leave-one-out' strategy is used to test the k -nearest-neighbours classification on the MIRCAB patient database (with the 9-dimensional reduced feature vector). Both computed and expert-selected optimal port configurations are tested. Table 3.5 summarizes the classification results and shows how varying k effects classification accuracy.

Table 3.5 – Nearest neighbour classification summary

Parameter k	1	3	5
Classification	15/17	14/17	14/17
Results	2 misses	3 misses	3 misses

3.5.4. Classifier comparison

Overall, classification of patient candidacy based on optimized feature geometry proved to be an effective measure for predicting successful and failed MIRCAB. For the Gaussian classifier, all of the failed cases were detected when using computed optimal port configurations. However, one of the successful cases was classified as a false-alarm

non-candidate and would have been operated on by conventional open-chest surgery if the algorithm was used. The Parzen window estimation resulted in the best classification results (for the particular $h_I = 0.5$): all non-candidates and candidates were classified correctly! Finally, the nearest neighbour classifier showed it always classified candidate patients correctly, but it could only detect 1/3 of the non-candidate cases. This is due to the small sample size of the failed cases ($N = 3$). For $k = 1$, one of the non-candidate patient geometries were most similar to other non-candidates. However, as k increased, the only possible k -nearest neighbours could be candidates. Perhaps if a larger sample size of failed MIRCAB cases was available, the nearest neighbour approach would improve in accuracy.

The two misclassification types hold implications on the risk of using statistical classification for predicting patient candidacy for MIRCAB. Patients who are in reality MIRCAB non-candidates, but who are classified as candidates (a 'miss') will undergo MIRCAB, but then be converted to conventional open-chest surgery. This error requires the patient to be subject only to minor additional risk. However, patients who are in reality MIRCAB candidates, but who are misclassified as a non-candidate (a 'false alarm'), will unnecessarily undergo conventional open-chest CABG when they could have received MIRCAB. This error is of greater concern – resulting in the unwanted risks of open-chest surgery. To improve classification outcomes, the comparative risk of each classification error could be accounted for by a loss function as described in Chapter sections 2.2.3.5-2.2.3.6.

3.6. Pre-operative planning summary

Port placement optimization algorithms were implemented and the resultant optimal port geometries were compared to expert chosen configurations. The algorithm could position port triads reliably with a small population-wide error of 13.7 ± 5.1 mm relative to expert chosen ports. Of course, the optimization cannot exactly match expert selections since computed optimal ports were chosen from a discrete port grid (in which the expert-chosen ports do not likely exist). Nonetheless, small port placement errors are tolerable: local expert surgeons confirm the slight variation in port positions would not affect the surgical outcome.

The computed optimal port configurations were, in addition, classified by pattern recognition techniques to test whether failed MIRCAB cases could be identified as non-candidates. The Parzen window estimation techniques proved that statistical classification could detect all incoming non-candidate cases even with a limited sample size. Notably, the sample size used in this thesis was very small. Hence, optimal feature values are not necessarily representative of the larger population, and could be improved by a larger sample size. In addition, undoubtedly, there are other factors not considered in the feature space that can cause failure (e.g. odd location and/or burial of the LAD). Statistical classification was demonstrated successfully on even this limited dataset. Certainly, with more trials, the classification algorithms would approach better accuracy and could incorporate more features. This thesis demonstrates that statistical classification can be used to identify MIRCAB patients from pre-operative images, but demands future investigations to find the best performing classification models. The work reveals a promising opportunity to build on MIRCAB patient databases for effective planning of port placement by optimization and patient candidacy classification.

Chapter 4. Intra-operative guidance: Laser projection for port placement

4.1. Intra-operative guidance overview

Transfer of pre-operative port placement plans to the patient in the operating room setting requires accurate intra-operative image-guidance systems. This chapter presents a novel application of an integrated optical tracking – laser projection system that displays port entry locations directly on top of the patient on the operating table. Registration of pre-operative images and the optical tracking system is performed using a set of landmarks visible in both the image and optical coordinates. Port placement configurations - chosen manually or computer optimized from pre-operative images - are then registered to the optical coordinates and are displayed by laser projection. Figure 4.1 shows a diagram of the image-guided surgery system. Accuracy of registration and port projection, limitations, and routine variations are covered through both: 1) system validation on a heart surgery phantom platform; and 2) four human case trials. Preliminary experiments leading to this work were published in [40], and are included in Appendix B.

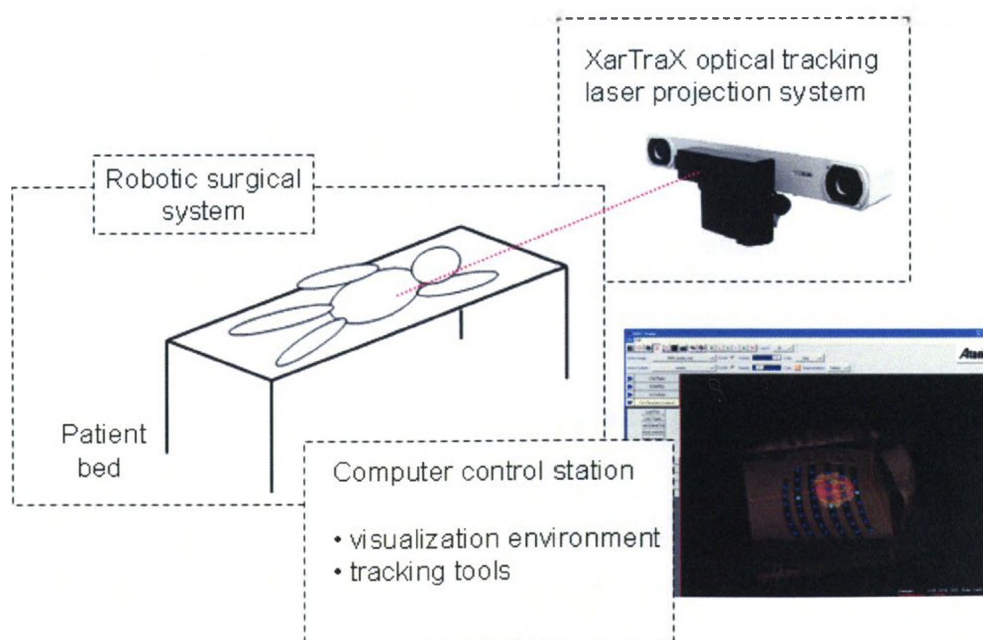


Figure 4.1 - Intra-operative image-guidance system diagram

4.2. Image-guidance system validation

A heart and chest cavity phantom was imaged and used to develop routines for registration and port placement laser projection. Experiments performed on the phantom system included: testing the improvement of 3D over 2D imaging for use in manual port placement mapping; comparing the accuracy of manual and laser projected port placement mapping (i.e. which system – human or machine – is more accurate at transferring the pre-operative image plans onto the patient); and, a complete accuracy assessment (registration and port placement) in an operating room setting.

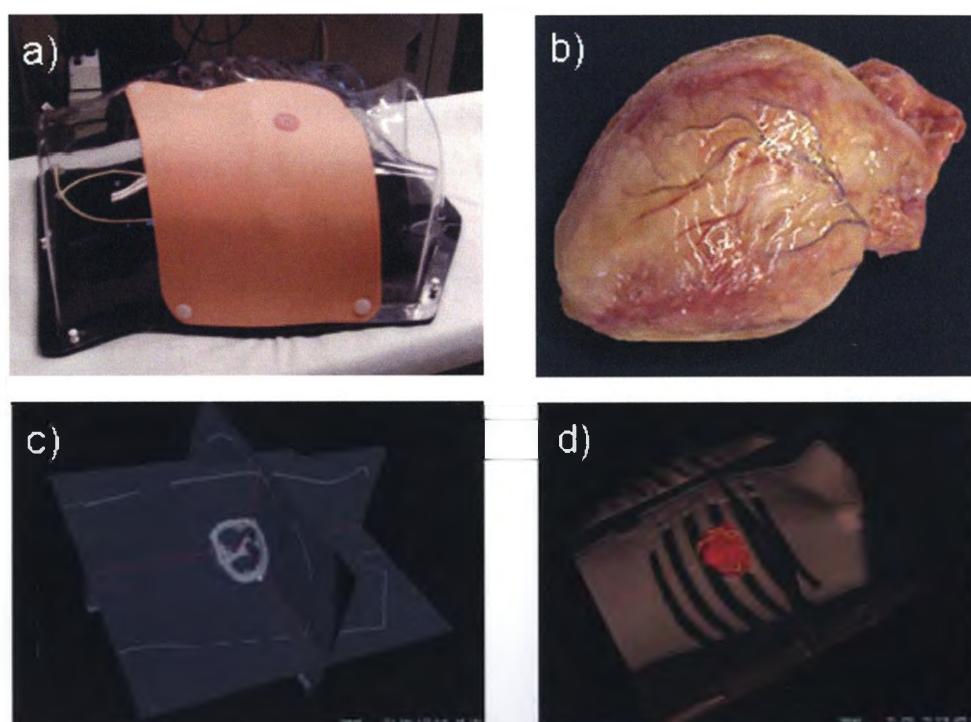


Figure 4.2 – The cardiothoracic phantom. Photographic images of: a) the phantom chest cavity and skin covering; and b) the heart. c) Tri-plane CT images of the phantom, and d) segmented surface reconstructions.

4.2.1. 2D vs. 3D image guidance: phantom manual port placement

4.2.1.1. Experiments

High-resolution 64-slice helical CT images (120 kV, 560 mA, FOV = 45 cm, matrix = 512×512 , slice thickness = 0.625 mm, imaging time = 9.5 s) were collected of the test phantom (The Chamberlain Group, MA). The phantom incorporated the following components specific for MIRCAB planning: a chest cavity, skin covering, a heart,

coronary arteries, and the LITA. Six CT-visible 1 mm Teflon bead fiducial markers were placed on the phantom for rigid-body registration. Photographic and CT images of the phantom are shown in Figure 4.2. In the following experiments, subjects (five novice volunteers and an expert robotic cardiac surgeon) were asked to transfer pre-operative port positions, located in the phantom image dataset, onto the physical phantom. Images were presented to the subject as either a scrollable stack of 2D images, or as a 3D tri-plane volume with surface segmentations. Figure 4.3 portrays how the port positions were indicated to the user in both the 2D and 3D images.

Five port configurations were pre-determined to evaluate 2D vs. 3D port placement mapping among novice and expert users. The port configurations, representative of past success geometries, were selected arbitrarily as their purpose was to test how well they could be physically mapped onto the imaged subject. Subjects were asked to locate the three port positions on the phantom by placing a pin at each port. Port placement mappings were tested for all five port configurations with both the 2D and 3D images. A trained system user performed registration beforehand, and measured the manually placed port coordinates using an active infra-red pointer with the Polaris optical tracking system.

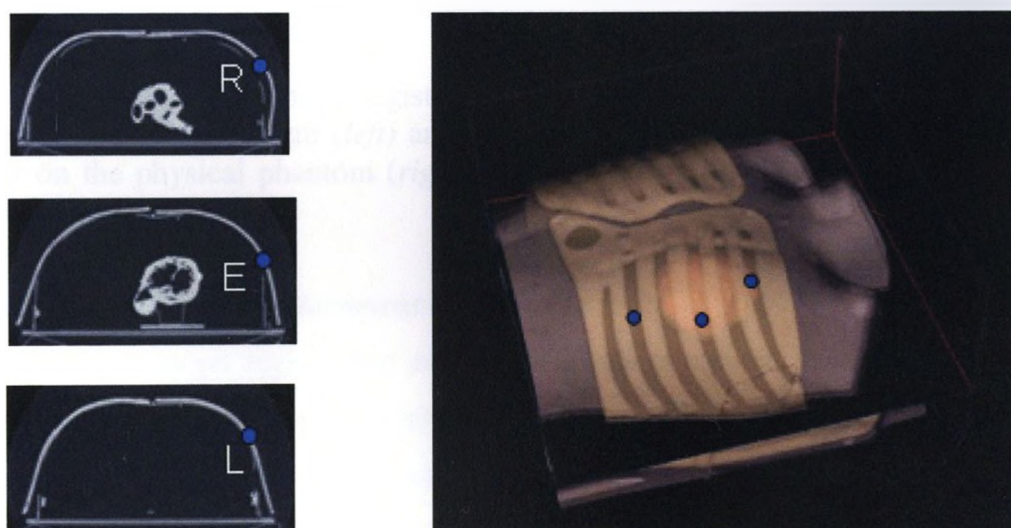


Figure 4.3 – 2D and 3D presentations for port placement. *Left:* Scrollable 2D images slices with port positions marked for the right (R), endoscopic (E), and left (L) operating tools. *Right:* Rotatable 3D surface images with the same port positions marked.

4.2.1.2 Results: Registration error

The fiducial registration error (FRE) was computed using the landmark positions from both the image and optical tracking coordinate systems. A trained system user performed the registration before each of the four novice and one expert manual port placement trials. Figure 4.4 shows the landmarks located on both the phantom and its volumetric image. The FRE for the manual phantom port placement experiments was 1.8 ± 0.4 mm ($N = 5$). This slight registration error is due to human imprecision in locating the exact centroid of the fiducial markers, both with the IR-pointer and in the image volume.

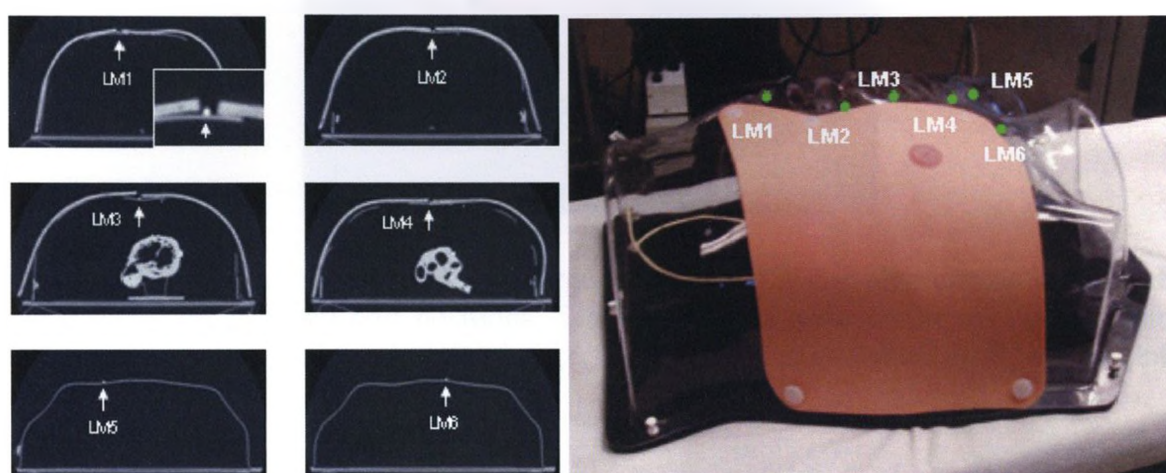


Figure 4.4 – Fiducial landmark registration. The six CT-visible landmarks are located in the image coordinate system (*left*) and are measured by an optically tracked active IR-pointer on the physical phantom (*right*) to solve for the image-world coordinate frame registration transformation.

4.2.1.3. Results: Port placement target error

The manual target registration error (TRE) was computed using the measured and image-based port placement coordinates. The optical tracking coordinates were registered to the image frame prior to evaluating the TRE. Figure 4.5 shows the registered coordinates of both the manual and image selected port configurations used for TRE evaluation. The error for manual port placement mapping was compared among 2D and 3D image plans, and among novice and expert users. Table 4.1 summarizes and compares the TRE for 2D and 3D based image guidance in novice and expert users. Note

that the FRE of 1.8 ± 0.4 is a very minor component of the calculated TRE. 3D image guidance improved port placement accuracy for both novice ($t_3 = 2.54$, $p < 0.05$, $N = 4$) and expert users ($N = 1$). In addition, manual port placement variability was also reduced in 3D image guidance compared to 2D guidance.

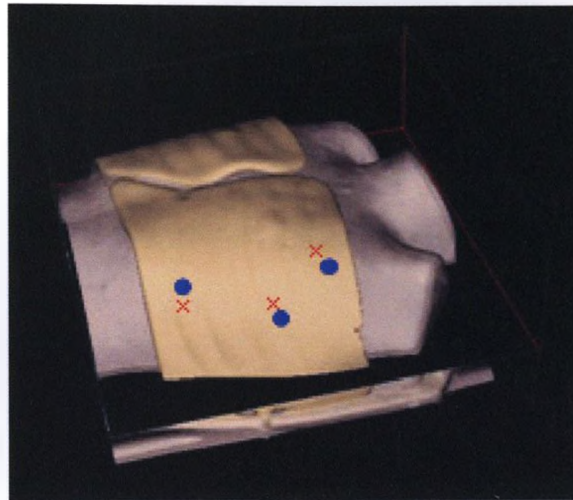


Figure 4.5 – Manual vs. image based target registration. The blue circles indicate the image based pre-selected port positions. The red crosses indicate the manually located port positions once registered to the image frame. TRE is evaluated from the distance error between the port position pairs.

Table 4.1 - 2D vs. 3D image-guided manual port placement error summary

Expertise	TRE _{2D} (mm)	TRE _{3D} (mm)
Novice ($N = 4$)	34.2 ± 12.1	19.3 ± 6.6
Expert ($N = 1$)	23.1	15.3

4.2.2. Image-guided phantom laser projection

4.2.2.1. Experiments

This section details the image-guided laser projection system and experimentation towards improved mapping of surgical port placement plans. The XarTraX system [13] was integrated into the Atamai image viewing software [28] to enable a port projection application. To begin use of the application, the user performs a landmark-based rigid

body registration. Landmarks in the image are located both in the Atamai viewing software and by the optical tracking system with use of an active IR pointer. Then, the application takes as input three image-based port coordinates (either manually selected or computer optimized), registers the coordinates to the optical tracking frame, and controls the laser projections to display over the port placement sites. The image-guided laser projection system was tested in a realistic operating room setting shown in Figure 4.6.

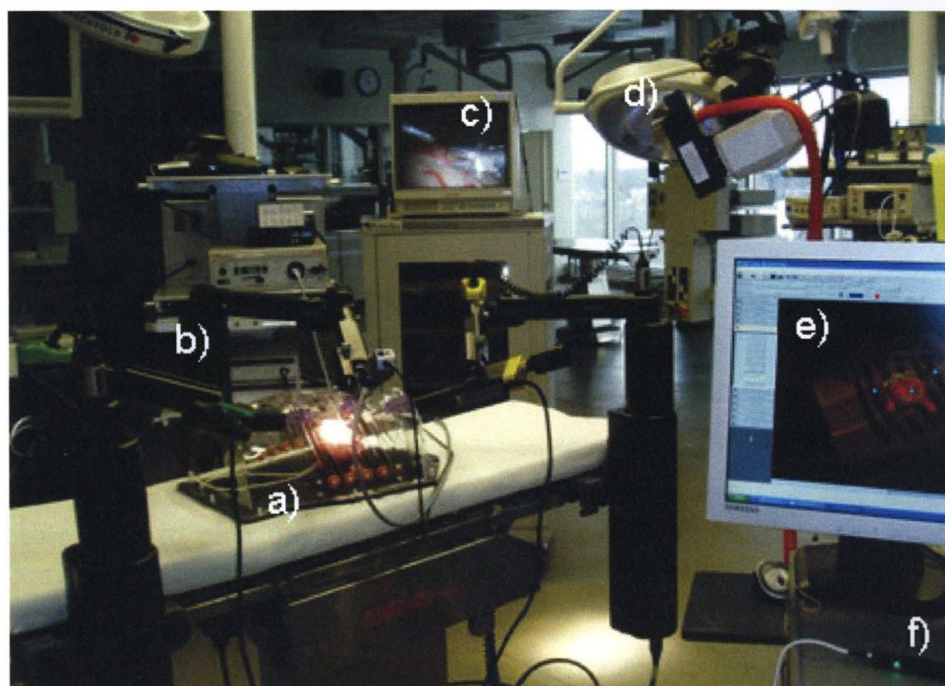


Figure 4.6 – Image-guided laser projection test bed: a) cardiothoracic phantom on the patient bed; b) Zeus surgical robot; c) video endoscope display; d) XarTraX optical tracking – laser projection system; e) Atamai Viewer visualization environment; and, f) active IR-pointer for registration.

Port placement plans mapped by laser projection were tested using the same five port configurations as in the manual port selection experiments. For each of the five configurations, port locations were projected and then measured by optical tracking. Port projections and their measurements were repeated three times at each port configuration, each repetition including a new fiducial registration. Figure 4.7 shows the port projections made on the phantom system.

4.2.2.2. Results: Registration and port placement error

The image-guided laser projection system accuracy was validated by comparing the measured and image-based port placement configurations. Prior to each projection trial, a new fiducial registration was performed. The image-based port coordinates were then registered to the optical tracking frame and are displayed by laser projection. An

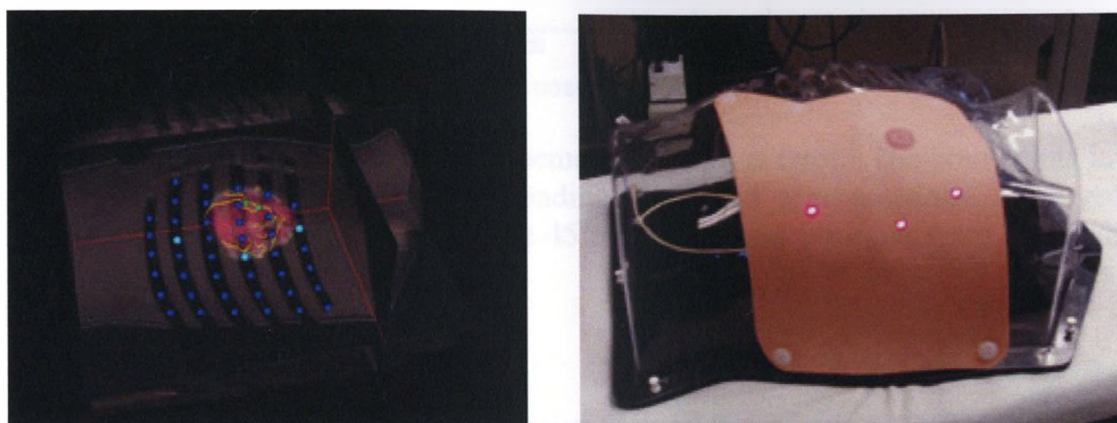


Figure 4.7 – Laser projected port placement on the phantom. *Left:* the 3D CT image of the phantom used to plan the port positions (*green* spheres among the blue port grid). *Right:* Example laser projection of the port positions (*red* laser spots on the skin).

active IR pointer in the optical frame was then used to measure the projected port positions. The per-trial port placement TRE was then computed by comparing the measured and registered image-based coordinates. Across all 45 laser projection port placement trials (three repeats \times three ports \times five configurations), overall system accuracy and precision is specified by the mean and standard deviation of the per-trial TRE. Figure 4.8 summarizes the system performance in terms of directional error components. The computed and measured port position were highly correlated. The higher z-component error is intrinsic to the optical tracking system. The computed TRE of 2.4 ± 0.4 mm was due mainly to registration ($\text{FRE} = 1.7 \pm 0.3$ mm, $N = 5$). Overall, the laser projection port placement mapping could be guided accurately within 2.5 mm ($t_{44} = 3.11$, $p < 0.05$).

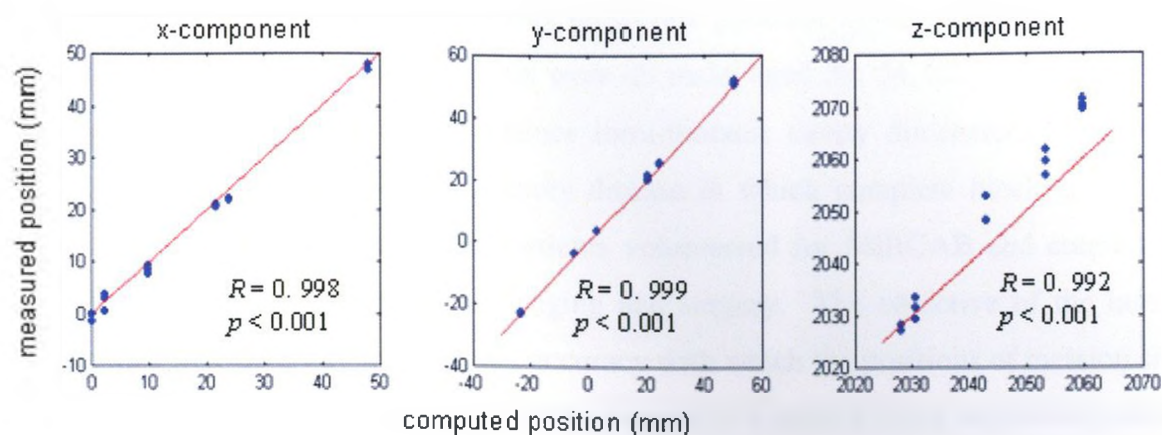


Figure 4.8 – Laser projection port placement directional error. The blue points indicate projection measurements for corresponding computed port positions. The red line indicates the line of equality. Note, the 45 port placement positions were not all distinct and thus overlap in the graphs.

4.2.3. Human vs. laser performance

Port placement mappings were superior with laser projection ($TRE = 2.4 \pm 0.4$ mm) than by human (best performance under expert 3D guidance showed $TRE = 15.3$ mm). The laser projection system eliminates manual sources of error in localizing port geometries, and reduces port mapping error to within 2.5 mm. Use of the image-guided laser projection system improved accuracy in mapping port placement plans, and warranted case studies to examine the system performance when faced with the natural geometric variation of patient-specific human trials.

4.3. Operating room evaluation: Human case studies

Conventionally, port placement is performed manually on the OR table. The surgeon, or an assistant, marks a line joining the top of the sternum (sternal notch) to the bottom of the sternum using a surgical marker. The intercostal spaces of each rib line are marked down the left side of the chest. Port positions are then selected, often among the 3rd, 5th, and 7th intercostal, by expert experience. The proposed augmented reality port placement device aims to map port positions – either selected manually within an image or computer optimized – onto the patient with sufficient accuracy to perform all the required surgical manipulations for MIRCAB.

Clinical feasibility for use of the laser projection guidance system was evaluated with four human case studies. The patients were all male, aged 39, 54, 52, and 46, and had varying upper-body physiques and hence intra-thoracic cavity dimensions. All were diagnosed with advanced coronary artery disease in which complete blockages of the LAD required bypass surgery. The patients volunteered for MIRCAB and entered the standard protocol for pre-operative imaging and surgery. The objective of the human case studies was to further evaluate the accuracy with which the positions of incision sites chosen from pre-operative images could be mapped to a patient using augmented reality laser projection under practical operating room conditions.

4.3.1. Pre-operative imaging

In each case, pre-operative breath-hold 4-slice CT (typically 120 kV, 1.5 mA, FOV = 45 cm, matrix = 256×256 , slice thickness = 1.125 mm, imaging time = 15.4 s) was performed. Fiducial markers were placed on bony landmarks (top of sternum, bottom of sternum, mid sternum, the most inferior point on the ribs, and above the nipple) to be used as registration markers in the OR. Additionally, to be used as port placement validation, three fiducial markers were placed on the intended port locations by an expert surgeon. Figure 4.9 shows the fiducial landmarks and marked port positions both on the patient and in the pre-operative CT images. Image-based coordinates of all landmarks and ports were located in the Atamai Viewer software, and 3D surface segmentation of the patient's ribs and skin were displayed to help plan the surgery. The images were inspected to manually determine candidacy for MIRCAB by an expert radiologist.

In the first trial, the patient was positioned flat on his back with both arms extended above their head, according to conventional CT Thorax imaging protocols. This imaging protocol, however, resulted in poor registration and laser projection in the OR: changes in the patient positioning during imaging and on the operating table must therefore be as similar as possible to enable intra-operative guidance. Image-guidance routines based on pre-operative images suffer from changes in patient positioning during surgery. Therefore, the expert surgeon should position the patient on the pre-operative imaging bed.

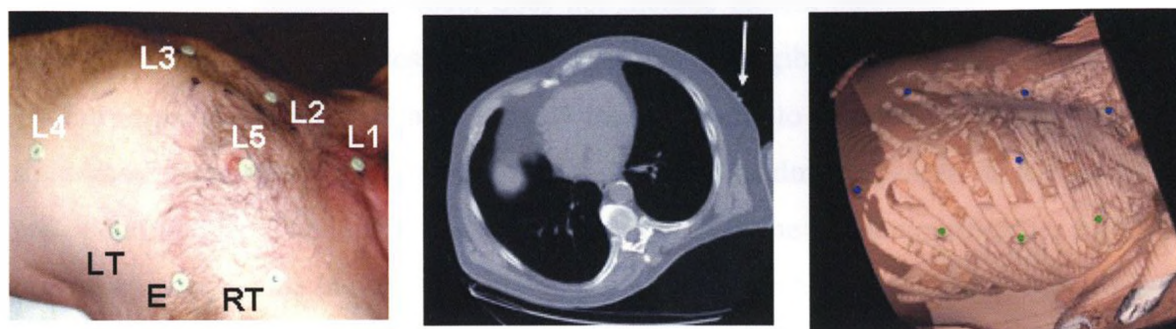


Figure 4.9 - Pre-operative fiducial markers and port placement on a patient. *Left:* Patient on the CT patient bed with fiducial markers placed at each of the five landmarks and at the three expert chosen port placement sites. *Centre:* CT slice of the patient tilted on a towel – as in surgery – with the arrow pointing to the CT-visible landmark. *Right:* Skin and rib reconstructions showing the landmarks (*blue*) and the port positions (*green*).

The following three patients were positioned by the cardiac surgeon as if they were on the operating table: tilted approximately thirty degrees up on their left side with a rolled sheet; left arm hanging limply down along the left side; and, right arm extended upwards over the head. Registration landmarks were placed at the rigid bony structures, and markers were placed manually at each of the port positions by conventional 3rd, 5th, and 7th approach. Patients were scanned one or two days in advance of their scheduled surgery and were asked to leave the markers on.

Ultimately, the objective of the case study experiments is to register the pre-operative 3D CT to the patient in the OR such that laser projected port positions are superimposed directly over the manually placed port markers. In this demonstration, the manually placed port landmarks, visible in the pre-operative images, serve as the image-based port position. Successful projection accuracy results would indicate that the image-guided laser projection could accurately transfer any port positions, whether chosen from the image, or optimized by an algorithm.

4.3.2. Experiments: Intra-operative registration and port projection

Over the four case studies, accurate mapping of the incision site was achievable with simple paired-point landmark registration. The first trial study demonstrates the misregistration and resultant shifting in the port placement projections that arises when

the pre-operative imaging protocol does not include patient positioning. The following three cases demonstrate successful projections with negligible error.

Intra-operative registration of the 3D image model to the patient was achieved by rigid-body paired-point registration using the fiducial landmarks placed on the patient for pre-operative CT. The landmarks were located both in the image coordinates, and in the optical tracking frame in the OR using an active IR pointer. Figure 4.10 shows the intra-operative registration routine. Some changes in patient geometry when placed on the operating table are unavoidable. In order to perform the robotic intervention, the chest cavity is insufflated and the left lung is deflated to create more intra-thoracic space for the robotic arms to operate. The deflation of the left lung results in a slight change in the chest's arc. Furthermore, the patient is anaesthetized for surgery. As a result, the left arm hangs limply to the patient's side and stretches the skin up towards the shoulder.



Figure 4.10 - Intra-operative registration routine. The expert surgeon points to each registration landmark on the patient corresponding to those marked in the image volume.

4.3.3. Results: Intra-operative registration and port projection

For each patient case, following registration, the pre-marked image-based port positions were registered to the optical frame and projected onto the patient. Then the

positions of the three projected ports were measured optically using an active IR pointer. Figure 4.11 shows image-guided laser projection in the OR, and subsequent insertion of robotic arms for MIRCAB. The per-patient FRE and TRE for all patient cases is summarized in Table 4.2. Note the higher FRE and TRE in the trial case due to poor patient positioning. Overall, the FRE for the well-positioned cases is due to both the user inability to locate a registration marker's centroid (in the image and on the patient), but more importantly changes in patient geometry. These changes in external patient geometry could be accounted for using more advanced nonlinear surface registration techniques to reduce registration error. Not accounting for changes in patient geometry resulted in increased FRE (6.3 ± 1.9 mm) and port projection TRE (7.7 ± 1.4 mm) – across the positioned patients – compared to that in phantom experiments (FRE = 1.7 ± 0.3 mm and TRE = 2.4 ± 0.4 mm).

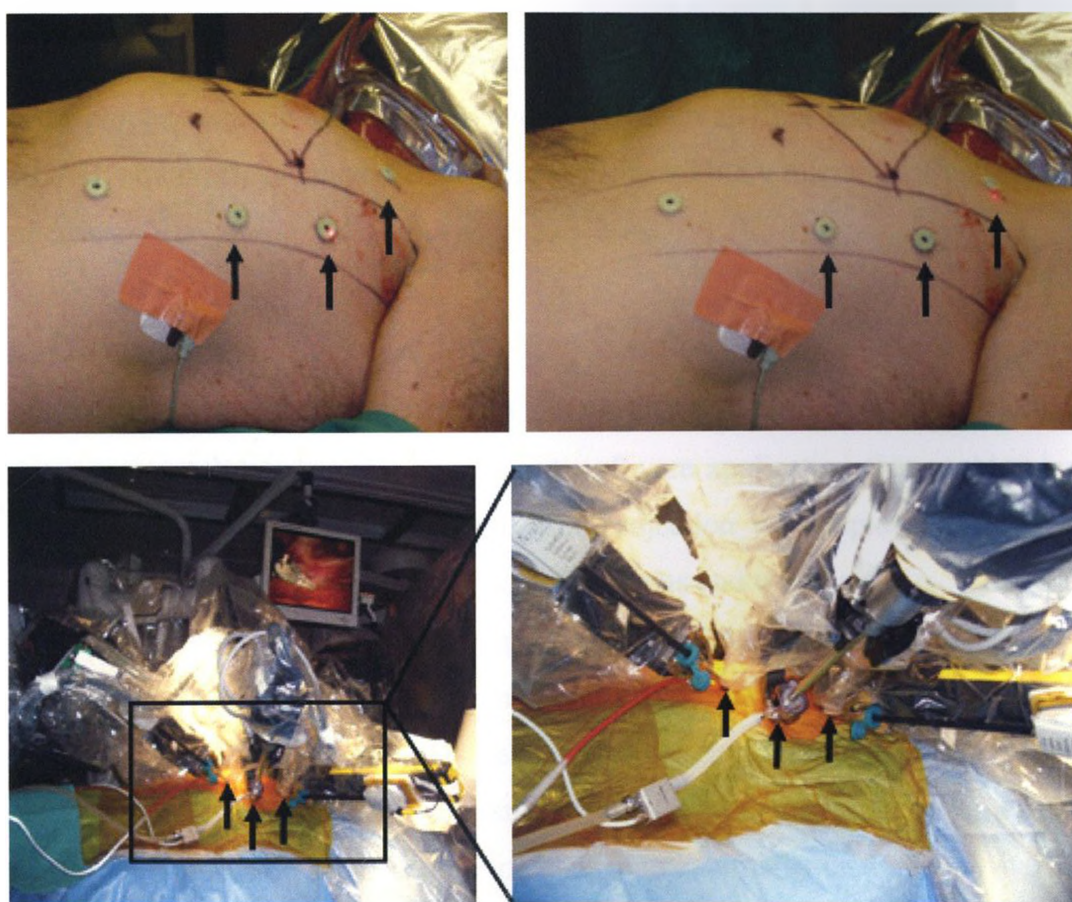


Figure 4.11 - Intra-operative laser projection for port placement. *Top*: Port placement laser projections. *Bottom*: insertion of the robotic arms.

Table 4.2 – Patient case study laser projection error summary

Case	Positioned (tilted for CT)	FRE (mm)	TRE (mm)
1	No	20.8	30.2
2	Yes	4.5	6.3
3	Yes	8.2	9.1
4	Yes	6.2	7.6

The case studies presented here show that the assumption for rigid-body registration, with proper positioning for pre-operative imaging, is sufficient to provide port placement projections within 1 cm ($t_2 = 2.88$, $p < 0.05$, $N = 3$ tilted patients): an error that is negligible in the current context. For example, a surgeon, given port positions projected slightly off target such that they lay over a rib, could manually correct the port locations to the center of the intercostal space. A surgeon choosing port positions under the conventional manual approach has no 3D context of the anatomy beneath the skin. The developed augmented reality projection overcomes this shortcoming in planning MIRCAB, and displays image-based port positions within a tolerable offset from optimal geometries.

4.4. Discussion

An augmented reality system for displaying port positions by image-guided laser projection was validated in this chapter. A software application that enabled landmark based registration and optically guided laser projection was implemented. The system accuracy was validated through phantom experiments and was then tested successfully on four human trials. Through bench-top phantom validation, 3D images proved more useful than 2D images for surgeons to map port placement plan, should they still choose a manual approach. Image-guided laser projection further enhanced the accuracy of mapping port placement plans. The system, when tested on patient cases, did suffer from some loss in registration accuracy due to changes in external patient anatomy. This error, nonetheless, was minimized to provide sufficient laser projected port placement guidance enabling safe access to all surgical sites for MIRCAB. Overall, the laser projection system integrated seamlessly into the OR and was easy to use before surgery.

Chapter 5: Conclusions and future work

A system for jointly planning and guiding MIRCAB interventions was implemented and tested in this thesis. Port placement optimization routines and a novel framework for classifying patient candidacy were presented for pre-operative planning. An augmented reality system was then developed and tested for intra-operative image-guided laser projection. Together, the planning and guidance routines serve as improved technology for: selecting candidate patients for MIRCAB based on pre-operative imaging; optimizing port placement plans; and accurate transfer of port placement plans to the patient in the OR. These are the primary care needs identified to ensure safe patient-by-patient based access to all surgical sites, reducing MIRCAB failures. Safe, effective, and reliable technologies that reproduce these successful surgical outcomes will ultimately enable minimally invasive surgery to become a more accessible procedure.

The implemented port placement optimization algorithm selected port triads with an error of 13.7 ± 5.1 mm relative to expert chosen ports. The error was due to variations in patient geometry relative to the expected geometry calculated from the database. Overall, the port placement optimization algorithm provided port selection appropriate for MIRCAB in all past successful patient cases. Future combination of the presented image-based optimization routines with other robot-dexterity based optimization routines [5,6] could provide a more robust port placement planning tool.

In testing the patient candidacy classification strategies, one of the major limitations was low patient sample numbers. For port placement optimization and patient candidacy assessment, seventeen patients were used, of which three were failed MIRCAB studies. A much larger sample space would provide more reliable classification results. Nonetheless, the demonstrated techniques were effective in identifying past failed cases. All of the tested classifiers – Gaussian, Parzen window, and k nearest neighbour – though showing a mix of ‘miss’ and ‘false alarm’ errors, improved the detection of non-candidate patients. More classification improvements could be made by: risk analysis of classification errors, sample size expansion, and advanced algorithm development. Future analysis of the risk implications of misclassification could be incorporated into the classification routines using a loss function. Also, in the long run, observed failures may

reveal more appropriate classification features (e.g. thoracic space volume from segmentation, thoracic proportions). Finally, development of advanced algorithms such as clustering techniques for identifying notable features [34] could improve classification accuracy. Effective classification will reduce conversion rates and enable routine successful MIRCAB.

The image-guided laser projection system was validated on a phantom test bed before patient trials. Experiments showed that 3D image-guidance improved port placement accuracy for both novices and experts, but laser projection was the most accurate method for mapping image-based port positions. Port projections were consistently within 2.5 mm of computed coordinates.

Intra-operative guidance for port placement using the augmented reality laser projection system was successful in three patient trials. However, port placement mappings suffered from remaining registration issues caused by changing geometry of the external patient anatomy. When the patient is anaesthetized on the OR bed, their left arm stretches further than when they are imaged consciously, and hence the registration markers shift between imaging and surgery. The present use of rigid-body landmarks could be improved by deformable surface registration techniques. This study shows sufficient registration accuracy enabled port placement mapping within 1 cm. This tolerance was acceptable for an expert surgeon to confirm or adjust as needed the port positions, and is comparable with other groups attempting OR transfer of MIRCAB plans [41]. A remaining cause of error in port placement optimization for the human cases that is not addressed is shifting of the heart following insufflation of the left lung. The port placement algorithm assumes the target locations on the heart when the patient is imaged by CT. However, following insufflation of the chest and deflation of left lung, the heart and target anatomy move relative to registration markers on the external anatomy. Future studies which account for movement of the heart following insufflation will improve the port placement optimization and registration in the OR. Work towards use of intra-operative trans-esophageal ultrasound for tracking the movement of the heart during collapsing of the lung and insufflation is underway. The intra-operative ultrasound images can be registered to pre-operative CT to correct for the heart movement due to

insufflation. Relocation of the LAD blockage site can then be used to update optimal port placement plans in the OR.

Clinical use of the proposed planning and guidance procedure will require further validation. Opportunity for growth in the patient optimization and classification database size will provide a more universal planning approach. Use of the port placement optimization and patient classification routine in conjunction with image-guided laser projection of pre-operative port placement plans is the desired paradigm, requiring the proposed integration of radiological and surgical protocols where the patient is positioned appropriately and fiducial registration markers are used. Future active trials where port placement configurations are computed from pre-operative images, then classified, then used for accurate image-guided laser projection, will afford assurance that the planning and guidance is robust and repeatable, and may be used on human patients for various minimally invasive robotic, laparoscopic and tele-surgical [42,43] interventions.

Appendix A – Research ethics approval

This appendix includes the approval of the Research Ethics Board protocol at the Lawson Health Research Institute for the patient robotic coronary bypass cases.

LAWSON HEALTH RESEARCH INSTITUTE
CLINICAL RESEARCH IMPACT COMMITTEE

RESEARCH OFFICE REVIEW NO.: R-08-333

PROJECT TITLE: An Optimal Planning Strategy for Robot-Assisted Minimally Invasive Cardiac Surgery

PRINCIPAL INVESTIGATOR: Dr. B Kiaii

DATE OF REVIEW BY CRIC: October 14, 2008

Health Sciences REB#: 15297

Please be advised that the above project was reviewed by the Clinical Research Impact Committee and the project:

Was Approved

PLEASE INFORM THE APPROPRIATE NURSING UNITS, LABORATORIES, ETC. BEFORE STARTING THIS PROTOCOL. THE RESEARCH OFFICE NUMBER MUST BE USED WHEN COMMUNICATING WITH THESE AREAS.

Dr. David Hill
V.P. Research
Lawson Health Research Institute

All future correspondence concerning this study should include the Research Office Review Number and should be directed to Sherry Paiva, Room C210, Nurses Residence, South Street Campus.

cc: Administration

Appendix B – Publication release

This appendix has been published in similar form in the Proceedings of Medicine Meets Virtual Reality 14 (2006) as part of Studies in Health Technology and Informatics [40].

Image-Guided Laser Projection for Port Placement in Minimally Invasive Surgery

Jonathan Marmurek^{1,2}, Chris Wedlake², Utsav Pardasani³, Roy Eagleson^{1,3}, Terry Peters^{1,2,3}

¹University of Western Ontario

²Robarts Research Institute

³Canadian Surgical Technologies and Advanced Robotics (CSTAR)
London, Ontario, Canada

Abstract. We present an application of an augmented reality laser projection system in which procedure-specific optimal incision sites, computed from pre-operative image acquisition, are superimposed on a patient to guide port placement in minimally invasive surgery. Tests were conducted to evaluate the fidelity of computed and measured port configurations, and to validate the accuracy with which a surgical tool-tip can be placed at an identified virtual target. A high resolution volumetric image of a thorax phantom was acquired using helical computed tomography imaging, and its 3D surface rendering was computed. Oriented within the thorax, a phantom organ with marked targets was visualized in a virtual environment. A graphical interface enabled marking the locations of target anatomy, and calculation of a grid of potential port locations along the intercostal rib lines. Optimal configurations of port positions and tool orientations were determined by an objective measure reflecting image-based indices of surgical dexterity, hand-eye alignment, and collision detection. Intra-operative registration of the computed virtual model and the phantom anatomy was performed using an optical tracking system. Initial trials demonstrated that computed and projected port placement provided direct access to target anatomy with an accuracy of 2 mm.

1 Introduction

Minimally invasive surgery (MIS), robotic or laparoscopic, is gaining popularity for use in a number of therapeutic procedures. Widespread practice of MIS, however, is limited by the lack of robust and flexible procedures for jointly planning and guiding optimal port placement. Additionally, accurate navigation of surgical end-effectors may enhance current endoscopic guidance techniques. Continuing advances in the quality of medical image acquisition, and developments in remote tracking systems, which can record motions of patients and surgical instruments, afford the opportunity to develop Image Guided Surgery (IGS) systems to assist surgeons. In MIS, systems which guide the

surgeon based on patient image data have the potential to optimize the intervention by ensuring appropriate port positions and tool trajectories, in addition to providing real-time virtual navigation of surgical instruments.

Previous work in port placement has focused on the modeling of optimization algorithms to determine the best incision sites for a patient-specific case. Adhami et al. [1] define an optimization problem based on indices of tool dexterity, visibility, target reachability, and surgeon comfort, and have shown successful results on animal trials. Specifically tuned for a Coronary Artery Bypass Graft (CABG) procedure, the optimization problem is refined by Selha et al. [2] such that port configurations attempt to match experimentally determined preset conditions. In addition, virtual environments have been developed [3,4] to display port configurations for robotic cardiac surgery.

Augmented reality (AR) systems designed to superimpose pre-operative planning information on top of the view of the surgical site have been developed to directly assist surgeons in addition to a virtual simulation. Glossop et al. [4] designed and tested an AR laser projection system which displayed pre-computed beam patterns for a simulated cranioanatomy, and Sugano et al. [5] have also used lasers in surgery to guide hip arthroplasty. To our knowledge, however, AR systems have not yet been reported for facilitating port placement.

This paper presents a novel application of augmented reality laser projection for port placement in minimally invasive surgery. Pre-operative image data are used to compute optimal incision sites and tool orientations. A 3D virtual simulation of the procedure is computed, and transferred to the operating room to offer the surgeon intra-operative guidance for port placement and end-effector navigation. We validate the accuracy of the proposed guidance system by comparing simulated and measured port placement trials on a phantom model.

2 Materials and Methods

2.1 Image Acquisition and Visualization

A high-resolution pre-operative volume of a thorax phantom was acquired with helical computed tomography imaging (slice thickness = 1.25 mm, pitch = 1.75, speed = 3.75 mm/rotation, field of view = 40 cm, kVp = 140 and mA = 160, imaging time = 54 sec, resolution = 512 x 512) on a GE Lightspeed Scanner. The dataset was stored as a 328 MB MINC file [7], and was further processed for visualization on a Desktop PC with commodity graphics.

The thorax phantom volume was visualized using an application based on Visualization ToolKit (VTK). Intensity CT data was examined using an interactive tri-planar display, allowing localization and thresholding of anatomy of interest. A surface segmentation and rendering of the ribs was computed using the marching cubes algorithm [8], and the isosurface was smoothed and decimated to a 28 MB VTK file of polygonal vertex positions and triangle normal vectors.

A foam sphere marked with coloured pins indicating assumed positions of target vasculature was used as a phantom organ in an example of a CABG procedure. The test organ was simulated in VTK, and was oriented within the intra-thoracic cavity of the ribs.

The computed virtual scene of the thorax phantom and test organ with marked targets was used as a patient-specific model on which to plan the surgical intervention.

2.2 Pre-Operative Optimal Planning

Pre-operative planning is used to identify and simulate optimal port configurations for minimally invasive interventions based on 3D pre-operative image data. We simulated a generic intra-thoracic MIS procedure in which two surgical tools are used in addition to one endoscope. The port placement problem, in this study, was to triangulate the 3D virtual coordinates for the three incision sites, in addition to computing and visualizing the required tool orientation for target access. Optimal port placement configurations, specified by triplets (n-tuples based on the number of operating instruments) of port position (x,y,z) and tool orientation (roll, pitch, yaw), were to facilitate and ensure repeatable collision-free access to multiple targets with satisfactory visibility, tool dexterity, and surgeon comfort.

Prior to optimization, a graphical interface was used to allow the user to navigate through 3D surfaces of the patient model, and to select target locations. Each target location was recorded by storing its 3D virtual coordinates (x,y,z) in addition to the normal vector (i,j,k) to the target surface. Next, a grid of potential port locations along the intercostal rib lines was defined (by manually selecting points in the volume). Potential ports were recorded by storing their 3D virtual coordinates and their vectors normal to the skin.

While higher sampling densities for port selection allow for more precise formulation of an optimal configuration, a larger set of potential ports creates a more exhaustive optimization search. For convenience, ports were placed 2-3 cm apart, but could be decreased to ~ 1 cm while maintaining reasonable computation time. The stored sets of targets and potential ports, along with the virtual geometric descriptions of the patient anatomy were then subject to seeking an optimal port configuration.

Implementation of the port-placement planning algorithm defined by Adhami et al. [3] was programmed in MATLAB, and was updated to use procedure-dependent preset optimal configurations, as shown by Selha et al. [2]. A discrete optimization problem was posed, to rank all potential configurations of one endoscope and two tools, by defining a 3-(n)-dimensional search space. All potential ports were numbered for indexing such that each cell in the search space showed an objective measure for an associated unique port configuration.

For each port configuration, the following geometric parameters were computed: port-to-port distances (d_{pp}), port-to-target distances (d_{pt}), tool-to-target normal angles (attack angles, α), and tool-to-skin normal angles (entrance angles, ϵ). Configurations were marked as 'admissible' if the computed parameters lay within the following constraints, respectively: minimum port separation ($d_{pp,min}$; to avoid placement redundancies), maximum tool shaft length (d_{ts}), maximum attack angle (α_{max} ; reflecting surgical requirements and tool tip dexterity), and maximum entrance angles (ϵ_{max} ; ensuring tolerable pressure against the ribs). Port admissibility was also constrained by a collision detection routine in VTK which ensures that each tool can reach all targets without obstruction.

An objective measure (Γ) was computed (by Eqn. 1) for each admissible port configuration, based on a summation the of least-squares difference between simulated attack angles (α) and optimal preset values (α^{opt}) for n surgical tools and m target sites. Hand-eye alignment weightings (ω) were applied to each objective score to ensure symmetry in the port configuration [3].

$$\begin{aligned} \min \quad & \Gamma = \omega \cdot \sum_{i=1}^n \sum_{j=1}^m (\alpha_{ij} - \alpha_{ij}^{opt})^2 \\ \text{s.t.} \quad & d_{pp} > d_{pp,min} \\ & d_{pt} < d_{ts} \\ & \alpha_{ij} < \alpha_{max} \\ & \varepsilon_{ij} < \varepsilon_{max} \end{aligned} \quad (1)$$

The final objective measures for each port configuration were ranked; indices of the highest ranked-ranked admissible cells indicated port positions and tool orientations for the optimal configurations.

2.3 Intra-Operative Guidance

In practice, transfer of the pre-operative plan to the operating room requires intra-operative registration of patient data and surgical tool motion in the virtual simulation to the real-world environment. Computed optimal port locations were registered to patient space using an optical tracking system, and were superimposed on the patient using a laser projection system. Motions of surgical instruments were mapped to the virtual environment by a second registration, allowing a user to align the simulated tool orientations with computed configurations to ensure optimal target access.

Registration. The virtual coordinates of four easily identifiable landmarks on the thorax phantom were recorded. The Polaris optical tracking system (NDI, Toronto, Canada), capable of measuring position and orientation data, was used to measure corresponding positions of physical landmarks by reading the tip position of an active IR-emitting pointer (Traxtal, Toronto, Canada) at each landmark. The spatial transformation mapping the virtual environment to the Polaris (real-world) coordinates was computed using Horn's method of absolute orientation [9].

Tracking and Projection. Coordinates of optimal port configurations were transformed to Polaris space, and were displayed on the thorax phantom using the XarTrax (Traxtal) laser positioning system (*Figure 1*). The XarTrax projector was mounted with the Polaris system, which simultaneously tracked motions of surgical tools and sampled positions of the laser spot to optimize the projection control [4]. A visible and an infrared laser were displayed by steering two galvanometrically controlled perpendicular mirrors. Laser positions were controlled by specifying angles of rotation for each mirror, using a built-in Application Programming Interface (API), common to both the Polaris and XarTrax control units.

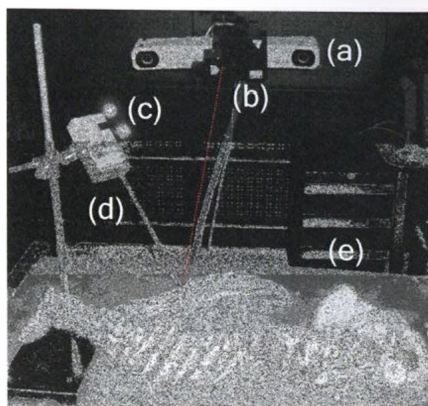


Figure 1 – Experimental setup for port placement and end-effector positioning: (a) Polaris tracking system; (b) XarTraX laser projector; (c) tracking tool; (d) in-lab robotic tool; (e) thorax phantom

2.4 Experiments

Accuracy validation trials were performed for: 1) port-placement configurations (port-position and tool orientation); and 2) end-effector tracking.

Port Placement. Computed and registered port positions and tool orientations were recorded for each of the five highest-ranked optimal port configurations. Using three ports per configuration, a total of 15 port positions were computed. For each simulated port position, the location (x,y,z) of the corresponding laser projected port was measured by an active IR-emitting pointer with the Polaris optical tracking system (rather than reading the laser spot location, pointer measurements mimicked surgical tool placement). *Figure 2* shows an example virtual port configuration and its intra-operative laser projection on the phantom. Next, an operating tool was registered to the virtual model and was aligned with computed port configurations. Tool orientation (roll, pitch, yaw) for each simulated port-placement trial were measured with a passive tracking tool attached to the surgical instrument.

End-Effector Tracking. Fifteen arbitrary targets were chosen in the simulated virtual space. The end-effector tool-tip of a registered surgical instrument was placed directly on each of the known physical targets, and simulated tool-tip positions were recorded (Note: this indication of error would be identical for the reverse experiment, in which the virtual tool-tips and targets are matched, as a surgeon would in practice, and then the real tool-tip positions are measured and compared to target locations).

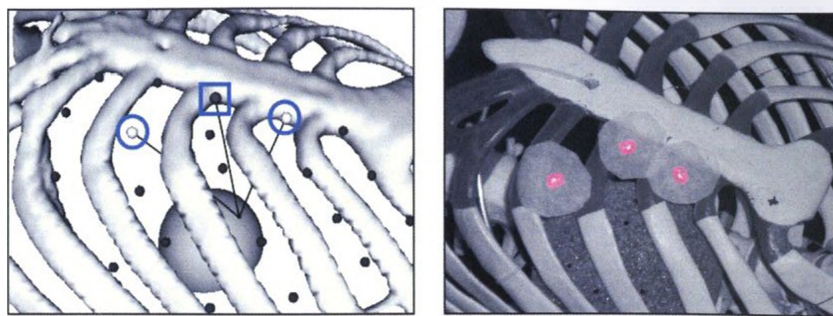


Figure 2 – *Left*: Simulated port configuration showing three highlighted ports which indicate computed optimal port positions for surgical instruments (circles) and an endoscope (square). Computed tool orientation is shown by a line connecting the port and the target. *Right*: Laser projection augmented reality guidance for port placement (bright spots near centre of tissue patches indicate optimal incision sites).

3 Results

A simple correlation measure demonstrated consistency between measured and computed optimal port configurations. *Figure 3* (top) shows scatter plots of measured vs. computed port locations positions, which estimate ‘zero error’ lines of equality. The computed and measured port positions were in agreement with high correlation coefficients in each direction: $R = 0.998$ in x , $R = 0.999$ in y , and $R = 0.992$ in z ($p < 0.001$). Similarly, as profiled in *Figure 3* (bottom), measured tool orientations were in agreement with the virtual simulation: $R = 0.994$ for roll, $R = 0.999$ for pitch, and $R = 0.978$ for yaw ($p < 0.001$).

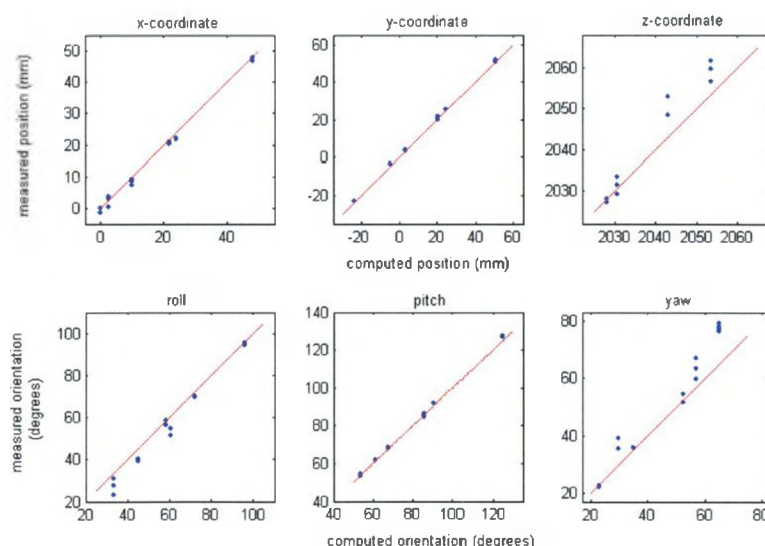


Figure 3 - Measured vs. computed port position (top) and tool orientation (bottom). The blue scatter plots show experimental data from the fifteen port placement trials (x , y , z , roll, pitch, and yaw for the three surgical tools from each of the five highest-ranked port configurations), which well estimate the red lines of equality.

Mean error and standard deviations are summarized in *Table 1* for port positions in each direction, and for the three degrees of tool orientation. Total error for port positions was computed by adding each orthogonal error component in quadrature (calculating Euclidean distance), while total error for tool orientation was computed as the angle between optimal and measured orientation.

Table 1 – Error summary from port placement validations trials

	Port Position Error (mm)				Tool Orientation Error (degrees)			
	x	y	z	Total	roll	pitch	yaw	Total
Mean	1.2	0.6	5.4	5.8	4.3	1.3	6.0	6.4
Std.	0.7	0.4	4.2	3.9	3.1	0.8	5.2	4.9

Port positioning and tool orientation results showed lowest accuracy and precision in the z-direction, and about the z-axis (yaw). This anisotropic error was likely due to the fall-off in tracking and projection precision as the distance increases from the Polaris-XarTrax unit. In the current application, we were only concerned with the x-y plane at the level of the rib cage. A single valued t-test was used to determine overall accuracy for both port positioning and tool orientation by testing mean total error of each. The system could provide accurate port position laser guidance within 1.7 mm and accurate tool orientation within 2.2 degrees ($t_{14} = 1.77$, $p < 0.05$).

Accuracy of end-effector tool-tip navigation is profiled in *Figure 4* by an ellipsoid indicating the 95 % confidence upper limit in which a tool-tip could be positioned, and by projections showing the bounding error in each plane. Mean error (Euclidean distance from the tool tip to the target) and standard deviation for the 15 targeting experiments in x, y, and z directions were 1.9 ± 1.4 mm, 1.5 ± 1.0 mm, and 2.5 ± 1.5 mm respectively.

4 Discussion

Intra-operative guidance of optimal port placement in minimally invasive surgery was achieved by superimposing laser projections of incision sites directly onto a test patient. A virtual simulation created from 3D pre-operative image data was used to plan the procedure, and to visualize port positions and tool orientations. Validation tests for port placement and subsequent end-effector navigation showed guidance with accuracy of 2 mm. These encouraging results warrant further developments and improvements on the current implementation. Automation of potential port selection using a centre-line detection algorithm will save planning time by reducing the amount user input. Additionally, an extensive database defining procedure-dependant preset optimal configurations will be developed through simulated surgical trials.

Clinical use of the proposed procedure will require further validation on case specific models. Opportunity to test the device on porcine subjects will afford assurance that the planning and guidance is robust and repeatable, and may be used on human patients for robotic, laparoscopic and telesurgical interventions.

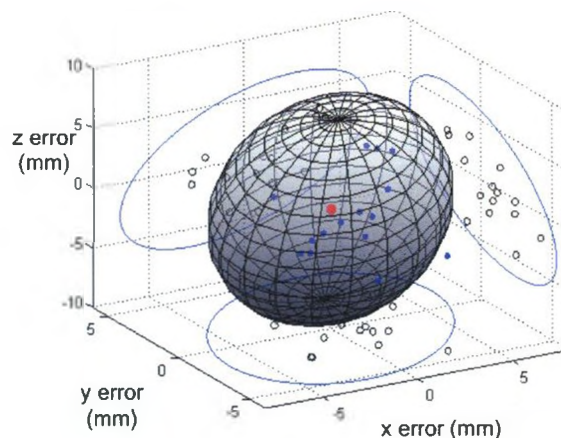


Figure 4 - Confidence ellipsoid for end-effector targeting. The red point indicates target locations normalized to the origin, and blue points mark the measured deviation from the end-effector tip positions to the target positions over fifteen trials. The ellipsoid shown represents the 95 % confidence boundary in which an end-effector tip can be guided ($p < 0.05$).

Acknowledgements

We wish to thank Edward Huang from the Robarts Research Institute for providing the CT scan used in this study, in conjunction with the London Health Sciences Centre. Funding for the project was made available by Ontario Research Development Challenge Fund (ORDCF).

References

1. Adhami, L., and Coste-Maniere, E.: Optimal planning for minimally invasive surgical robots. *IEEE Trans. on Robotics and Automation* (2003) October Vol 19, no. 5: 854-862.
2. Selha, S., Dupont, P., Howe, R., and Torchiana, D.: Dexterity optimization by port placement in robot-assisted minimally invasive surgery," 2001 *SPIE International Symposium on Intelligent Systems and Advanced Manufacturing*, Newton, MA, 28-31 October (2001).
3. Traub, J., Feuerstein, M., Bauer, M., Schirmbeck, E.U., Najafi, H., Bauernschmitt, R., and Klinker, G.: Augmented reality for port placement and navigation in robotically assistive minimally invasive cardiovascular surgery. *International Congress Series* (2004) 1268: 735-740.

4. Chiu, A.M., Dey, D., Drangova, M., Boyd, W.D., and Peters, T.M.: 3-D Image Guidance for Minimally Invasive Coronary Artery Bypass. Heart Surgery Forum. (2001) [Online]. Available: <http://www.hs-forum.com/vol3/issue3/2000-9732.html>
5. Glossop, N., Wedlake, C., Moore, J., Peters, T.M., and Wang, Z.: Laser Projection Augmented Reality System for Computer Assisted Surgery. MICCAI-2003 (2003) 1-8.
6. Sugano, N., Sasama, T., Nishihara, S., Nakase, S., Nishii, T., Miki, H., Momoi, Y., Yoshinobu, S., Nakajima, Y., Tamura, S., Yonenobu, K., and Ochi, T.: Clinical applications of a laser guidance system with dual laser beam rays as augmented reality of surgical navigation, in: Lemke, H.U. et al. (Eds.). Proc. 16th Int. Congress and Exhibition on Computer Assisted Radiology and Surgery (CARS), Springer (2002): 281.
7. Neelin, P.D., MacDonald, D., Collins, D.L., Evans, A.C.: The MINC file format: from bytes to bairs. Neuroimage (1998) 7(4):S786.
8. Lorensen, W.E., and Cline, H.E.: Marching cubes: A high resolution 3D surface construction algorithm. ACM Computer Graphic (1987) Vol 21:163-169.
9. Horn, B.K.P.: Closed-form solution of absolute orientation using unit quaternions. Journal of the Optical Society of America (1987) Vol 4:629-641.

References

- [1] W.D. Boyd, R. Rayman, N.D. Desai, A.H. Menkis, W. Dobkowski, S. Ganapathy, B. Kiaii, G. Jablonsky, F.N. McKenzie, R.J. Novick. *Closed-chest coronary artery bypass grafting on the beating heart with the use of a computer-enhanced surgical robotic system*. Journal of Thoracic Cardiovascular Surgery. 2000; 120: 807-809.
- [2] L. Adhami, E. Coste-Maniere. *Optimal planning for minimally invasive surgical robots*. IEEE Transactions on Robotics and Automation. 2003; 19/5: 854-863.
- [3] S. Selha, P. Dupont, R. Howe, D. Torchiana. *Dexterity optimization by port placement in minimally invasive surgery*. SPIE Symposium on Intelligent Systems and Advanced Manufacturing. 2001.
- [4] A.H. Menkis, K. Kadera, B. Kiaii, S.A. Swinamer, R. Rayman, W.D. Boyd. *Robotic surgery, the first 100 cases: Where do we go from here?* Heart Surgery Forum. 2004; 7(1): 1-4.
- [5] A.L. Trejos, R.V. Patel. *Port Placement for Endoscopic Cardiac Surgery Based on Robot Dexterity Optimization*. Proceedings of the 2005 IEEE International Conference on Robotics and Automation. 2005: 912-917.
- [6] A.L. Trejos, R.V. Patel, I. Ross, B. Kiaii. *Optimizing port placement for robot-assisted minimally invasive cardiac surgery*. The International Journal of Medical Robotics and Computer Assisted Surgery. 2007; 3/4: 355-364.
- [7] J.W. Cannon, J.A. Stoll, S.D. Selha, P.E. Dupont, R.D. Howe, D.F. Torchiana. *Port placement planning in robot-assisted coronary artery bypass*. IEEE Transactions on Robotics and Automation. 2003; 19/5: 912-917.
- [8] F. Devernay, F. Mourgues, E. Coste-Maniere. *Towards endoscopic augmented reality for robotically assisted minimally invasive cardiac surgery*. Proceeding of the International Workshop on medical Imaging and Augmented Reality. 2001: 16-20.
- [9] V. Falk, F. Mourgues, L. Adhami, S. Jacobs, H. Thiele, S. Nitzsche, F.W. Mohr, E. Coste-Manière. *Cardio Navigation: Planning, Simulation, and Augmented Reality in Robotic Assisted Endoscopic Bypass Grafting*. Annals of Thoracic Surgery. 2005; 79: 2040-2047.
- [10] G.A. Turgeon, G. Lehmann, G. Guiraudon, M. Drangova, D. Holdsworth, T. Peters. *2D-3D registration of coronary angiograms for cardiac procedure planning and guidance*. Medical Physics. 2005; 32/12: 3737-3749.

- [11] A.M. Chiu, D. Boyd, T.M. Peters. *3-D visualization for minimally invasive robotic coronary artery bypass (MIRCAB)*. Engineering in Medicine and Biology Society, 2000. Proceedings of the 22nd Annual International Conference of the IEEE. 2000; 3: 1728 – 1730.
- [12] R. Bauernschmitt, M. Feuerstein, J. Traub, E.U. Schirmbeck, G. Klinker, R Lange. *Optimal port placement and enhanced guidance in robotically assisted cardiac surgery*. Surgical Endoscopy. 2007; 21/4: 684-687.
- [13] M. Feuerstein, S.M. Wildhirt, R. Bauernschmitt, N. Navab. *Automatic patient registration for port placement in minimally invasive endoscopic surgery*. Medical Image Computing and Computer Aided Intervention. 2005; 8/2: 287-94.
- [14] V. Falk, F. Mourgues, T. Vieville, S. Jacobs, D. Holzhey, T. Walther, F.W. Mohr, E. Coste-Manière. *Augmented reality for intraoperative guidance in endoscopic coronary artery bypass grafting*. Surg Technol Int. 2005; 14: 231-5.
- [15] N. Glossop, C. Wedlake, J. Moore, T.M. Peters, Z. Wang. *Laser projection augmented reality system for computer assisted surgery*. MICCAI. 2003: 1-8.
- [16] N. Sugano, T. Sasama, S. Nishihara, S. Nakase, T. Nishii, H. Miki, Y. Momoi, S. Yoshinobu, Y. Nakajima, S. Tamura, K. Yonenobu, T. Ochi. *Clinical applications of a laser guidance system with dual laser beam rays as augmented reality of surgical navigation*. CARS. 2002: 281.
- [17] D. West, A.C. De Souza, J. Pepper. *Robotic coronary artery surgery*. The British journal of Cardiology. 2003; 10: 52-55.
- [18] M.R. Katz, J.O. Bonatti. *Totally endoscopic coronary artery bypass grafting on the arrested heart*. Heart Surgery Forum. 2007; 10(4): E338-43.
- [19] W.D. Boyd, B. Kiaii, R.J. Novick, R. Rayman, S. Ganapathy, W.B. Dobkowski, G. Jablonsky, F.N. McKenzie, A.H. Menkis. *RAVECAB: improving outcome in off-pump minimal access surgery with robotic assistance and video enhancement*. Canadian Journal of Surgery. 2001; 44(1): 45-50.
- [20] M. Bashkirov. *Pro: robotically-assisted CABG is the optimal treatment for coronary artery disease*. Journal of Cardiothoracic and Vascular Anesthesia. 17/4: 546-548.
- [21] R.C. King, T.B. Reece, J.L. Hurst, K.S. Shockey, C.G. Tribble, W.D. Spotnitz, I.L. Kron. *Minimally invasive coronary artery bypass grafting decreases hospital stay and cost*. Annals of Surgery. 1997; 225(6): 805-9.

- [22] R.S. Poston, R. Tran, M. Collins, M. Reynolds, I. Connerney, B. Reicher, D. Zimrin, B.P. Griffith, S.T. Bartlett. *Comparison of economic and patient outcomes with minimally invasive versus traditional off-pump coronary artery bypass grafting techniques*. Annals of Surgery. 2008; 248(4): 638-46.
- [23] V. Subramanian, N.U. Patel, N.C. Patel, D.F. Loulmet. *Robotic assisted multivessel minimally invasive direct coronary artery bypass with port-access stabilization and cardiac positioning: Paving the way for outpatient coronary surgery?* Annals of Thoracic Surgery. 2005; 79: 1590-1596.
- [24] W.F. Turner, J.H. Sloan. *Robotic-assisted coronary artery bypass on a beating heart: initial experience and implications for the future*. Annals of Thoracic Surgery. 2006; 82: 790-794.
- [25] J. Bonatti, T. Schachner, O. Bernecker, O. Chevtchik, N. Bonaros, H. Ott, G. Friedrich, F. Weidinger, G. Laufer. *Robotic totally endoscopic coronary artery bypass: Program development and learning curve issues*. Journal of Thoracic Cardiovascular Surgery. 2004; 127: 504-510.
- [26] A. Oehlinger, N. Bonaros, T. Schachner, E. Ruetzler, G. Friedrich, G. Laufer, J. Bonatti. *Robotic Endoscopic Left Internal Mammary Artery Harvesting: What Have We Learned After 100 Cases?* Annals of Thoracic Surgery. 2007; 8(3): 1030-1034.
- [27] R.J. Novick, S.A. Fox, B.B. Kiaii, L.W. Stitt, R. Rayman, K. Kodera, A.H. Menkis, W.D. Boyd. *Analysis of the learning curve in telerobotic, beating heart coronary artery bypass grafting: 90 patient experience*. Annals of Thoracic Surgery. 2003; 7: 749-753.
- [28] Atamai Interactive Visualization. <<<http://www.atamai.com/>>>.
- [29] The McConnell Brain Imaging Centre of the Montreal Neurological Institute. *MINC*. <<<http://www.bic.mni.mcgill.ca/software/minc/>>>.
- [30] W.E. Lorensen, H.E. Cline. *Marching Cubes: A high resolution 3D surface construction algorithm*. Computer Graphics (SIGGRAPH 1987 Proceedings). 1987; 21(4): 163-170.
- [31] M.J. Magee, M.J. Mack. *Robotics and coronary artery surgery*. Current Opinion in Cardiology. 2002; 17(6): 602-7.
- [32] F.W. Mohr, V. Falk, A. Diegeler, T. Walther, J.F. Gummert, J. Bucerius, S. Jacobs, R. Autschbach. *Computer-enhanced "robotic" cardiac surgery: experience in 148 patients*. Journal of Thoracic and Cardiovascular Surgery. 2001 May; 121(5): 842-53.

- [33] D. de Cannière, G. Wimmer-Greinecker, R. Cichon, V. Guliernos, F. Van Praet, U. Seshadri-Kreaden, V. Falk. *Feasibility, safety, and efficacy of totally endoscopic coronary artery bypass grafting: multicenter European experience*. Journal of Thoracic and Cardiovascular Surgery. 2007 Sep; 134(3): 710-6.
- [34] R.O. Duda, P.E. Hart, D.G. Stork. *Pattern Classification*. (2nd Ed.). Wiley & Sons: New York. 2001.
- [35] B.K.P. Horn. *Closed-form solution of absolute orientation using unit quaternions*. Journal of the Optical Society of America. 1987; 4(4): 629-642.
- [36] P.J. Besl, N.D. McKay. *A Method for registration of 3-D shapes*. IEEE Transaction on Pattern Analysis and Machine Intelligence. 1992; 14(2): 239-256.
- [37] J.M. Fitzpatrick, J.B. West, C.R. Maurer. *Predicting error in rigid-body point-based registration*. IEEE Transaction on Medical Imaging. 1998; 17(5): 694-702.
- [38] G. Reiter, U. Reiter, P. Bergmann, R. Rienmuller. *MR-imaging based port placement planning for totally endoscopic coronary artery bypass grafting*. Interactive Cardiovascular and Thoracic Surgery. 2004; 3(2): 341-5.
- [39] P. Bergmann, S. Huber, H. Segl, H. Maechler, U. Reiter, G. Reiter, R. Reinmuller, P. Oberwalder, B. Rigler. *Cardiac MR in robotic heart surgery for preoperative identification of the target vessel and precise port placement – a theoretical model*. Thoracic and Cardiovascular Surgery. 2003; 51(4): 204-10.
- [40] J. Marmurek, , C. Wedlake, U. Pardasani, R. Eagleson, T. Peters. *Image-guided laser projection for port placement in minimally invasive surgery*. Studies in Health Technology and Informatics. 2006; 119: 367-72.
- [41] E. Coste-Maniere, L. Adhami, F. Mourgues, O. Bantiche, D. Le, D. Daunt, N. Swarup, K. Salisbury, G. Guthart. *Optimal planning of robotically assisted heart surgery: transfer precision on the operating room*. Experimental Robotics. 2003; 5: 424-434.
- [42] R. Rayman. K. Croome, N. Galbraith, R. McClure, R. Morady, S. Peterson, S. Smith, V. Subotic, A. Van Wynsberghe, S. Primak. *Long-distance robotic telesurgery: a feasibility study for care in remote environments*. International Journal of Medical Robotics. 2006; 2(3): 216-24.
- [43] Q. Liu, R.J. Scibassi, A. Kassam, F. Zhu, R. Machessault, G. Gilbert, M. Sun. *An overview of 3D video transmission and display technologies for telemedicine applications*. Studies in Health Technology and Informatics. 2007; 125: 298-303.